









# Exploring the Origin of Ultralong Gamma-Ray Bursts: Lessons from GRB 221009A

Amit Kumar Ror<sup>1,2</sup> , Rahul Gupta<sup>1,3,8</sup> , Amar Aryan<sup>1,4</sup> , Shashi Bhushan Pandey<sup>1</sup>, S. R. Oates<sup>5</sup> ,  
A. J. Castro-Tirado<sup>6,7</sup> , and Sudhir Kumar<sup>2</sup> 

<sup>1</sup> Aryabhata Research Institute of Observational Sciences (ARIES), Manora Peak, Nainital-263001, India; [amitror@aries.res.in](mailto:amitror@aries.res.in), [rahulbhu.c157@gmail.com](mailto:rahulbhu.c157@gmail.com), [shashi@aries.res.in](mailto:shashi@aries.res.in)

<sup>2</sup> Department of Applied Physics/Physics, Mahatma Jyotiba Phule Rohilkhand University, Bareilly-243006, India

<sup>3</sup> Astrophysics Science Division, NASA Goddard Space Flight Center, Mail Code 661, Greenbelt, MD 20771, USA

<sup>4</sup> Graduate Institute of Astronomy, National Central University, 300 Jhongda Road, 32001 Jhongli, Taiwan

<sup>5</sup> Physics Department, Lancaster University, Bailrigg, Lancaster LA1 4YB, UK

<sup>6</sup> Instituto de Astrofísica de Andalucía (IAA-CSIC), Glorieta de la Astronomía s/n, E-18008, Granada, Spain

<sup>7</sup> Departamento de Ingeniería de Sistemas y Automática, Escuela de Ingenierías, Universidad de Málaga, C. Dr. Ortiz Ramos sn, E-29071, Málaga, Spain

Received 2024 March 19; revised 2024 May 26; accepted 2024 June 3; published 2024 August 14

## Abstract

The brightest gamma-ray burst (GRB) ever, GRB 221009A, displays ultralong GRB (ULGRB) characteristics, with a prompt emission duration exceeding 1000 s. To constrain the origin and central engine of this unique burst, we analyze its prompt and afterglow characteristics and compare them to the established set of similar GRBs. To achieve this, we statistically examine a nearly complete sample of Swift-detected GRBs with measured redshifts. We categorize the sample to bronze, silver, and gold by fitting a Gaussian function to the log-normal of  $T_{90}$  duration distribution and considering three subsamples respectively to 1, 2, and 3 times of the standard deviation to the mean value. GRB 221009A falls into the gold subsample. Our analysis of prompt emission and afterglow characteristics aims to identify trends between the three burst groups. Notably, the gold subsample (a higher likelihood of being ULGRB candidates) suggests a collapsar scenario with a hyperaccreting black hole as a potential central engine, while a few GRBs (GRB 060218, GRB 091024A, and GRB 100316D) in our gold subsample favor a magnetar. Late-time near-IR observations from 3.6 m Devasthal Optical Telescope rule out the presence of any bright supernova associated with GRB 221009A in the gold subsample. To further constrain the physical properties of ULGRB progenitors, we employ the tool MESA to simulate the evolution of low-metallicity massive stars with different initial rotations. The outcomes suggest that rotating ( $\Omega \geq 0.2 \Omega_c$ ) massive stars could potentially be the progenitors of ULGRBs within the considered parameters and initial inputs to MESA.

*Unified Astronomy Thesaurus concepts:* [Gamma-ray bursts \(629\)](#); [Astronomy data analysis \(1858\)](#); [Black holes \(162\)](#); [Magnetars \(992\)](#)

*Materials only available in the [online version of record](#): machine-readable tables*

## 1. Introduction

Gamma-ray bursts (GRBs) are characterized by intense and short-lived bursts of high-energy (a few keV–MeV) radiation. GRBs emit electromagnetic radiation in two phases. The first phase, known as “prompt emission,” typically persists for a duration ranging from a few milliseconds to several thousands of seconds (Kumar & Zhang 2015; Pe’er 2015). The presence of bimodality in the duration ( $T_{90}$ )<sup>9</sup> distribution of the prompt emission of GRBs has led to the classification of these events into two distinct categories (Kouveliotou et al. 1993): long-duration ( $T_{90} \geq 2$  s) and short-duration ( $T_{90} \leq 2$  s) GRBs. Long GRBs (LGRBs) have been observed to originate from the demise of the core collapse of massive stars (Woosley 1993; Hjorth et al. 2003). Conversely, short GRBs (SGRBs) have been attributed to mergers involving compact objects such as neutron stars–neutron stars or a neutron star–black hole (Perna & Belczynski 2002; Abbott et al. 2017). In addition to these

two traditional classes, a unique and intriguing class known as ultralong GRBs (ULGRBs) has been suggested. These exceptional events defy the conventional timescales associated with standard GRBs, exhibiting durations (several thousands of seconds) far beyond what is typically observed. However, the finding of Virgili et al. (2013), Levan et al. (2014), Boër et al. (2015), Levan (2015), and Perna et al. (2018) suggest that there is no precise boundary to separate LGRBs and ULGRBs. Even though not all the GRBs are considered ULGRBs based on their prompt emission duration, in some cases, the combined duration in gamma-ray/hard X-ray and soft X-ray (flares or plateau) is utilized to separate between the two classes (Zhang et al. 2014). Unlike the duration of ULGRBs, the total fluence exhibited by these events is not an exception. This fluence stretched over a longer timescale, requiring a highly sensitive instrument for their detection (Levan et al. 2014). Further, some of the well-studied ULGRBs (GRB 060218 and GRB 100316D) are found to be intrinsically soft, posing energy constraints on the detecting instruments. The orbital constraints associated with space-based detectors also present challenges in capturing the complete emissions of ULGRBs (Levan 2015). Swift’s remarkable sensitivity in soft energy channels and its unique observation strategy, both in the event rate and integrated image mode, have proven beneficial in detecting several ULGRBs (Gehrels et al. 2004). However, despite the discovery of numerous well-classified ULGRBs such as GRB 060218, GRB 091024A,

<sup>8</sup> NASA Postdoctoral Program Fellow.

<sup>9</sup> It refers to the duration encompassing 5%–95% of the fluence observed in soft gamma/hard X-ray channels.



GRB 100316D, GRB 101225A, GRB 111209A, GRB 121027A, GRB 130925A, GRB 141121A, GRB 220627A, and many more over the years, our understanding of their progenitors, central engine, and the surrounding environments remains elusive (Virgili et al. 2013; Evans et al. 2014; Levan et al. 2014; Boër et al. 2015; Levan 2015; Perna et al. 2018; Gendre et al. 2019; de Wet et al. 2023).

Direct evidence regarding the progenitors of ULGRBs emerges from the observation of associated supernovae (SNe) accompanying these long-lasting events. These observations strongly imply that the demise of massive stars (collapsar) may account for some ULGRBs (Campana et al. 2006; Starling et al. 2011; Thöne et al. 2011; Nakauchi et al. 2013; Greiner et al. 2015). However, alternative explanations are also proposed as potential progenitors capable of launching long-lasting ultrarelativistic jets: (1) The tidal disruption of a white dwarf by a black hole has been proposed as a potential progenitor for ULGRBs (Campana et al. 2011). According to Ioka et al. (2016), under specific circumstances, such an occurrence could give rise to the SN-like features observed in the late afterglow light curve of ULGRBs. (2) A massive star ( $15\text{--}30 M_{\odot}$ ) with low metallicity, possessing a rotation that culminates in its evolution into a blue supergiant (BSG), represents a potential progenitor for ULGRBs. BSG stars, characterized by significantly larger radii compared to Wolf-Rayet (W-R) stars, can collapse into hyperaccreting black holes. This scenario offers a natural explanation for the unexpectedly prolonged durations observed in ULGRBs (Perna et al. 2018). (3) Another contender for the progenitor of ULGRBs is a highly magnetized millisecond pulsar, often referred to as a magnetar (Usov 1992). The energy released during the spin-down of a magnetar can play a significant role in the formation of a bipolar jet, and such a mechanism holds promise in elucidating the long-lasting emission observed in ULGRBs (Bucciantini et al. 2007, 2009).

In recent years, significant progress in both observational technology and theoretical modeling has illuminated our understanding of ULGRB progenitors. The Modules for Experiments in Stellar Astrophysics (MESA) code (Paxton et al. 2011, 2013, 2015, 2018, 2019; Jermyn et al. 2023), a highly robust tool for modeling stellar evolution, has played a pivotal role in these advancements. Perna et al. 2018 utilized MESA to evolve stars with masses of  $30 M_{\odot}$  and  $40 M_{\odot}$  under varying initial rotation conditions. Their findings demonstrated that moderately rotating massive stars could culminate their evolution as BSG, which can successfully launch an ultra-relativistic jet to power ULGRBs. Moreover, Song & Liu (2023) conducted a comprehensive exploration of the impact of initial mass, metallicity, and rotation on magnetar formation. This extensive study involved evolving 227 stellar models using MESA. In this context, we leverage MESA to distinguish between the progenitors of LGRBs and ULGRBs by evolving massive stars within the mass range of  $15\text{--}30 M_{\odot}$  while considering various initial rotation scenarios. The minimum mass limit for typical LGRB progenitor given by Larsson et al. (2007) is  $20 M_{\odot}$ . However, modeling results of Perna et al. (2018) revealed BSG stars as the progenitors of ULGRBs. The standard mass of BSG stars is  $15 M_{\odot}$  (Dessart & Hillier 2018). Therefore, we select  $15 M_{\odot}$  as our starting point. The choice of minimum mass  $15 M_{\odot}$  is also supported by Bromberg et al. (2011). The upper limit of  $30 M_{\odot}$  is motivated from Perna et al. (2018) and Song & Liu (2023). Therefore, we use a mass range

of  $15\text{--}30 M_{\odot}$  while evolving the massive star models in MESA and all related analyses.

Efforts have also been made to account for the observed duration of ULGRBs by examining the properties of the surrounding medium rather than solely focusing on unique central engines or progenitors. As proposed by Evans et al. (2014), it is suggested that the circumburst environment of ULGRBs may distinguish them from LGRBs. ULGRBs could potentially be situated within exceedingly low-density surroundings, resulting in a deceleration of their ejecta at a slower rate compared to a denser medium. Until now, ULGRBs have shown diverse observed characteristics during the prompt emission and afterglow phases. For example, observed SNe emission associated with GRB 060218, GRB 100316D, and GRB 111209A (Campana et al. 2006; Starling et al. 2011; Greiner et al. 2015), the association of GRB 101225A, GRB 111209A, and GRB 121027A with active star-forming galaxies and exhibiting a mixed type of surrounding environment (Levan et al. 2014). Most ULGRBs exhibit early X-ray light curves featuring flares or plateau (Zhang et al. 2014), and in some cases, they show thermal components in early X-ray afterglow. However, all such properties are common in LGRBs or low-luminous GRBs. Consequently,  $T_{90}$  stands out as the robust parameter distinguishing ULGRBs from the broader LGRB population. Therefore, considering  $T_{90}$  as a separation criterion, we statistically examine a subsample of ULGRB candidates from the complete set of Swift-detected bursts. This work investigates the underlying physical mechanism, possible progenitors, and central engine contributing to their unexpectedly long duration compared to LGRBs and SGRBs.

The Gamma-ray Burst Monitor (GBM; Meegan et al. 2009) on board Fermi Gamma-ray Space Telescope (hereafter Fermi) and the Burst Alert Telescope (BAT; Barthelmy et al. 2005) on board Swift-detected GRB 221009A, which stands out as the brightest (surpasses nearby monster GRBs such as GRB 130427A and GRB 190114C in terms of observed fluence and isotropic energy release) burst ever observed (Lesage et al. 2023). Remarkably, Fermi-GBM recorded emission from this burst for over 1000 s (Lesage et al. 2023), and Konus-Wind reported a soft tail emission that extended up to an astonishing 20,000 s (Frederiks et al. 2023), thereby positioning it as a potential candidate as a ULGRB (Burns et al. 2023; Frederiks et al. 2023). In this work, we thoroughly studied the characteristics of this burst and compared it to a larger sample of ULGRB candidates. Additionally, LHAASO and Carpet-2 missions have claimed the detection of photons with energies of 18 TeV (Y. Huang et al. 2022) and 250 TeV (Fraija et al. 2022), respectively. With this, GRB 221009A has become the first ULGRB candidate to belong to the class of very high-energy (VHE, few hundred GeV–TeV) GRBs (Ror et al. 2023).

This paper is structured as follows: Section 2 presents our selection criteria for bronze, silver, and gold subsamples of ULGRBs candidates that we investigate. In Section 3, we analyze the multiwavelength characteristics of GRB 221009A and compare them to those of a broader sample of ULGRBs. Section 4 describes the basic characteristics, possible progenitors, and central engines of the GRBs included in our sample. The simulations of massive stars with MESA code are given in Section 5, and Section 6 provides the summary and conclusion.

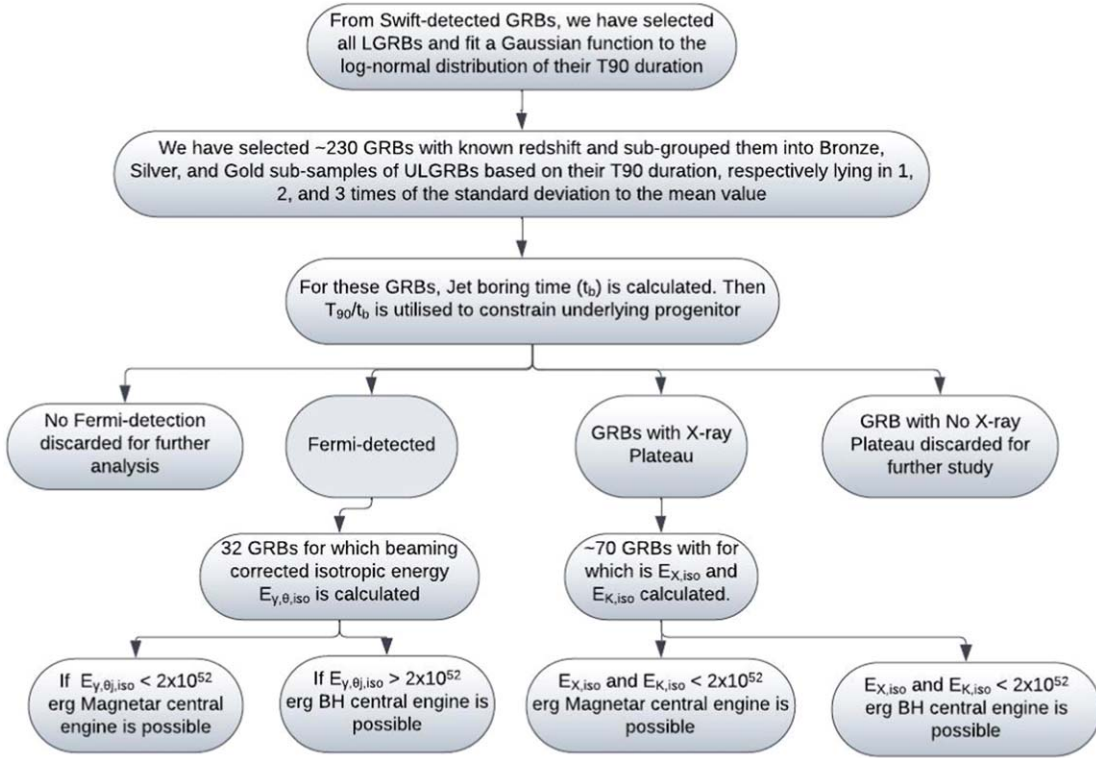


**Figure 1.** Description/flow chart of the methods used to select the bronze, silver, and gold subsamples and to constrain their possible progenitors and central engines.

## 2. Sample Selection and Methodology

Due to the limitations of duration-based classification, there is no exact boundary between LGRBs and ULGRBs. The different sensitivities of space-based gamma-ray detectors at different energies and orbital constraints can lead to the omission of significant amounts of prompt emission from some GRBs (Levan 2015). For instance, Konus-Wind observed three emission episodes for ULGRB GRB 091024A, while Swift only detected the first episode, resulting in a shorter  $T_{90}$  duration (Virgili et al. 2013). Consequently, it becomes imperative to establish a uniform sample selection methodology for conducting comprehensive analyses of ULGRBs. Motivated by this, we searched for possible candidates for ULGRBs in the complete sample of Swift-detected bursts.<sup>10</sup> However, our selection methodology extends beyond merely considering GRBs with durations exceeding a few thousands of seconds. Our detailed sample selection approach and the methodology to constrain the possible progenitor and the central engine are described in Figure 1.

- Initially, we constructed a log-normal distribution representing the  $T_{90}$  durations of a complete sample (from 2005 to 2023) of Swift-detected GRBs,<sup>11</sup> which unveiled a bimodal pattern. For those GRBs listed as ULGRBs in Swift catalog,<sup>12</sup> we have used  $T_{90}$  duration from the third Swift-BAT catalog (Lien et al. 2016). This is because bursts with longer durations are most likely to

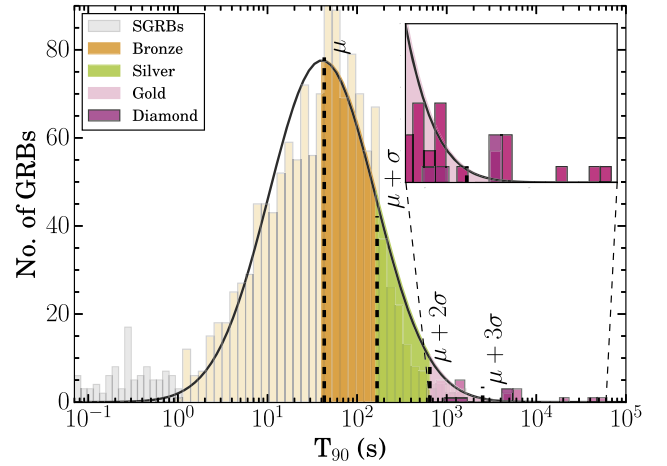


**Figure 2.** Represents the  $T_{90}$  distribution of Swift-detected LGRBs. The orange, green, and pink shaded regions represent the bronze, silver, and gold subsamples of ULGRBs. The inset magnifies the region that represents the gold subsample, and additional magenta bars represent the diamond subsample. The black dashed lines are plotted at  $\mu = 43$  s,  $\mu + \sigma = 167$  s,  $\mu + 2\sigma = 649$  s, and  $\mu + 3\sigma = 2519$  s.

have emissions beyond the event data range (photons detected in  $T_{0,BAT}-250$  s to  $T_{0,BAT}+950$  s, where  $T_{0,BAT}$  is the BAT trigger time). Lien et al. (2016) analyzed the BAT survey data and provided the complete duration for these bursts, combining the event and survey data. The observed bimodality exhibited one peak associated with SGRBs and another with LGRBs. In our pursuit of ULGRB candidates, we deliberately omitted the peak associated with the SGRBs, as illustrated in Figure 2.

- We fitted a Gaussian function to the distribution of Swift-detected LGRBs. To create our ULGRB sample, we exclusively chose GRBs with  $T_{90}$  durations greater than

<sup>10</sup> In this paper, we utilize  $T_{90}$  as the criteria to discriminate between the various categories of GRBs and to compare their prompt and afterglow emission characteristics. We do not claim this is the only criterion for distinguishing ULGRB candidates from other SGRBs and LGRBs.

<sup>11</sup> [https://swift.gsfc.nasa.gov/results/batgrbeat/index\\_tables.html](https://swift.gsfc.nasa.gov/results/batgrbeat/index_tables.html)

<sup>12</sup> [https://swift.gsfc.nasa.gov/results/batgrbeat/summary\\_cflux/summary\\_GRBlist/list\\_ultra\\_long\\_GRB\\_comment.txt](https://swift.gsfc.nasa.gov/results/batgrbeat/summary_cflux/summary_GRBlist/list_ultra_long_GRB_comment.txt)

the mean of the distribution, denoted as  $\mu$  (with  $\mu = 43$  s). There are  $\sim 740$  GRBs with  $T_{90} > 43$  s. In order to compute the true energetics, we require these GRBs to have redshift, which reduces the sample down to 230 GRBs (see Table A1). We further subdivided the sample into bronze, silver, and gold subsamples through divisions in  $T_{90}$  durations. Bronze, silver, and gold bursts fall within the ranges of  $(\mu - \mu + \sigma)$ ,  $(\mu + \sigma - \mu + 2\sigma)$ , and  $(\mu + 2\sigma - \mu + 3\sigma)$  or beyond, respectively.

- Furthermore, to ensure comprehensiveness, we have incorporated well-studied instances of GRBs with  $T_{90} > 1000$  s (that are not included in our bronze, silver, and gold subsamples) from the existing literature and put them in the diamond subsample. A detailed description of these ULGRB candidates is given in Table A2.

The yearly distribution of our bronze, silver, and gold subsamples is depicted in the upper panel of Figure 3. We have shown the cumulative distribution of redshift of the bronze, silver, and gold subsamples in the bottom panel of Figure 3. We noted that the cumulative distribution of the gold + diamond subsample does appear at a lower redshift with respect to our bronze and silver subsamples, mainly due to selection effects. The typical fluence observed from ULGRBs is not very different from LGRBs (Levan 2015). This observed fluence distributed over a longer timescale makes several ULGRBs faint. Therefore, these events are difficult to detect at higher redshift due to instrumental sensitivities or observational constraints. Consequently, detecting them at lower redshifts is more feasible, whereas only a few bright ULGRBs may be detectable at higher redshifts.

### 3. Comparison among the Characteristics of Sample GRBs

In this section, we compare the temporal and spectral characteristics of GRBs in our bronze, silver, and gold subsamples.

#### 3.1. Machine-learning Technique to Differentiate between Subsamples

We have used a machine-learning tool,  $t$ -distributed stochastic neighbor embedding ( $t$ -SNE), developed by Garcia-Cifuentes et al. (2023), to find differences between our selected subsamples and other LGRBs and SGRBs detected by Swift-BAT until 2023 December.  $t$ -SNE processes the high-energy light curve of GRBs and, based on similarities and dissimilarities between the light curves, places them in a 2D map by forming a cluster of points where similar events lie close. The axes of this 2D map do not have any significance. However, labeling each event with redshift and  $T_{90}$  using different colors or markers allows us to observe their impact on grouping within the map. The clustering between two groups representing the bimodal distribution of GRBs (SGRBs and LGRBs) was observed by Jespersen et al. (2020) using the  $t$ -SNE method.

To download and process the Swift-BAT data (GRBs detected up to 2023 December) with  $t$ -SNE, we follow the procedures given in Garcia-Cifuentes et al. (2023).  $t$ -SNE map of the Swift-detected GRBs along with GRBs in the gold, silver, and bronze subsample highlighted is shown in Figure 4. In this figure, the bronze, silver, gold, and diamond subsamples are represented by orange, green, red, and magenta colors,

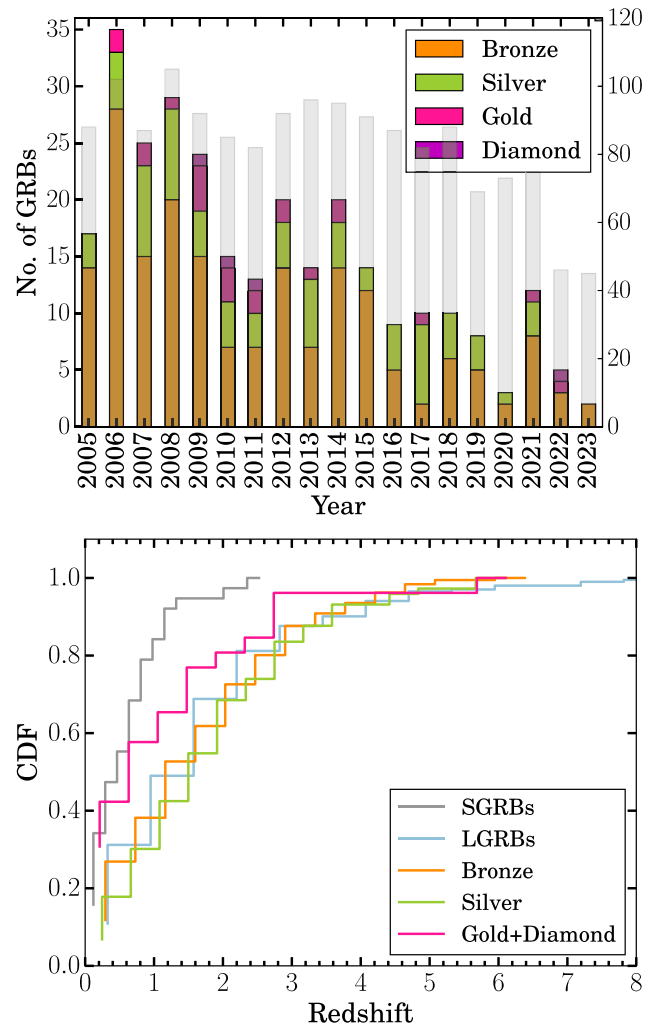


**Figure 3.** Upper panel represents the year-wise distribution of our bronze, silver, gold, and diamond samples of ULGRBs detected up to 2023 December. The histogram plot of all Swift-detected GRBs is shown in the background with gray color bars. The drop in long-duration GRBs ( $T_{90} > 43$  s) over time might reflect the aging of BAT instruments, and the number of enabled detectors has decreased significantly over the years due to their permanently noisy behavior (Moss et al. 2022). On the other hand, Swift has conducted a significantly greater number of slews to observe more targets in recent years, resulting in shorter exposure times for each pointing. Given that many ULGRBs exhibit faint and longer emissions, detecting them becomes more challenging with shorter exposure times. The bottom panel represents the cumulative distribution of redshift of the bronze, silver, and gold+diamond subsamples.

respectively. Since our bronze, silver, gold, and diamond subsamples represent the light curves of different durations, we expect different clustering of these events by  $t$ -SNE. From the Figure 4, we noted that the silver subsample GRBs mostly lie on the left of the map and gradually decrease toward the right. Similarly, the gold and diamond subsample also tends to cluster on the left of the map; however, five GRBs (GRB 070518  $T_{90} \sim 5.5$  s, GRB 090309A  $T_{90} \sim 3.0$  s, GRB 090404  $T_{90} \sim 82$  s, GRB 091127  $T_{90} \sim 7.42$  s, and GRB 101024A  $T_{90} \sim 18.7$  s) lying on the right are considered in our gold/diamond subsample based on the duration given in Lien et al. (2016). GRB 221009A lies at the top left edge of the map, indicating the ultralong nature of the burst. The detailed physical implications of the obtained results are given below.

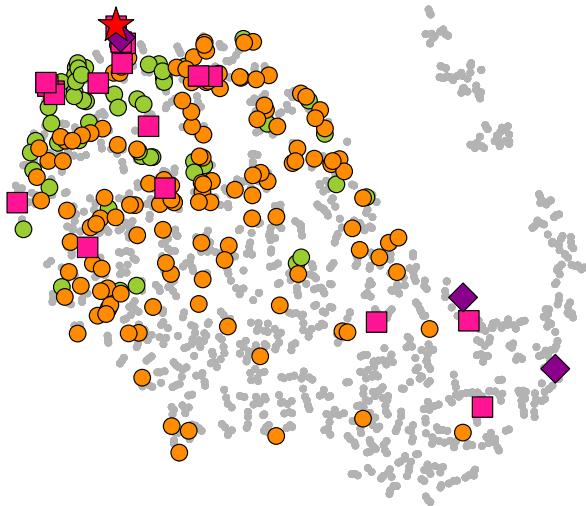


**Figure 4.**  $t$ -SNE distribution map for Swift-BAT GRBs 64 ms binned light curves are grouped into two main classes. Green and orange colored circles represent our silver and bronze subsamples, respectively. Red and magenta squares represent the gold and diamond subsamples. GRB 221009A is shown with a red star.

Utilizing the  $t$ -SNE map as a tool to discern between different classes of GRBs based on their observed prompt emission light curves, we made several notable observations. First, we observed that LGRBs and SGRBs are distinctly segregated into the bulk and tail regions of the  $t$ -SNE map, respectively. This clear grouping suggests that SGRBs exhibit prompt emission light curves that are fundamentally different from those of LGRBs, and both of these classes have different physical origins. However, upon closer examination, we found that the light curves of the bronze subsample do not exhibit any discernible structural differences compared to LGRBs. Instead, they are uniformly distributed among the LGRBs. The uniform distribution indicates that the selected features used for the  $t$ -SNE analysis do not effectively discriminate between bronze subsample and LGRBs, as expected. Furthermore, we noticed that GRBs in the silver and gold subsamples predominantly cluster on the left side of the  $t$ -SNE map. This clustering suggests that the prompt emission light-curve morphologies of these subclasses may differ from those of LGRBs, and they might have different physical origins. However, it is worth noting that some GRBs in the gold and diamond subsamples also appear on the right side of the map. This occurrence is primarily due to observation constraints; only a short portion of their light curve is utilized in the grouping. Our analysis revealed that the  $t$ -SNE grouping is primarily based on temporal features of observed light curves and does not adequately distinguish between different subclasses based on the activity of the central engine. Consequently, relying solely on light-curve morphology for the distinction between different GRB classes may be only partially appropriate. Therefore, in the subsequent sections, we utilize other methods to distinguish the characteristics of different sample subclasses.

### 3.2. High-energy Characteristics of Sample GRBs

The prompt identification of ULGRBs is crucial for in-depth observational and theoretical investigations. We utilize the spectral characteristics of GRBs in bronze, silver, and gold subsamples and search for potential differences from other GRBs of well-studied subclasses such as LGRBs with

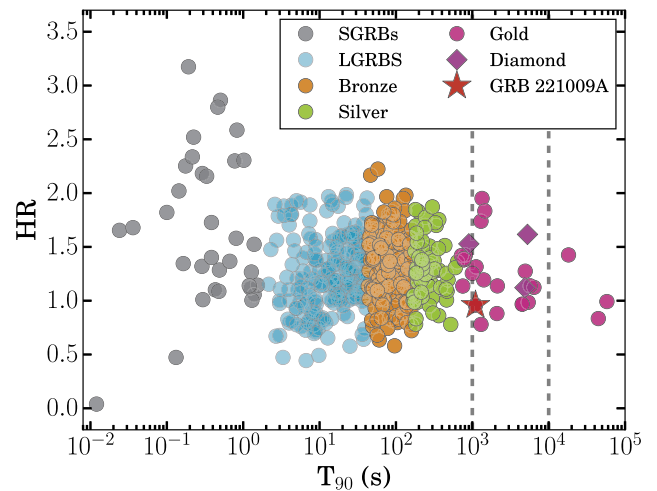


**Figure 5.** The hardness ratio in the Swift-BAT 50–100 keV/25–50 keV bands for our selected subsamples is plotted with the burst’s duration ( $T_{90}$ ). Two vertical gray lines at  $\sim 10^3$  and  $10^4$  s represent the proposed demarcation of  $T_{90}$  duration between LGRBs and ULGRBs as published by Boër et al. (2015) and Levan (2015), respectively.

$T_{90} < 43$  s (as  $T_{90} > 43$  s included in our bronze subsample) and SGRBs. We calculated the hardness ratio (HR) for each GRB in our sample by comparing the fluence in the hard energy range (50–100 keV) to that in the soft energy range (25–50 keV). Figure 5 illustrates the distribution of HR as a function of  $T_{90}$  for all the bursts. We noted that GRBs in the gold subsample exhibit lower average hardness values. GRB 221009A also lies toward the softer ends of HR.

In the upper panel of Figure 6, we have shown the distribution of fluence in 15–150 keV along with their durations. We found an increasing trend in the fluence with durations of the burst from SGRBs to GRBs in our bronze and silver subsamples. However, gold and diamond subsamples do not seem to follow the trend. GRB 221009A is the brightest ever burst with observed fluence  $\sim 0.09$  erg cm $^{-2}$  (GBM; Lesage et al. 2023) and  $\sim 10^{-4}$  erg cm $^{-2}$  (BAT 15–150 keV, Evans et al. 2007, 2009). Since the gold and diamond subsamples show similar properties, from now on, we will present the combined properties of these two subsamples.

In the middle panel and the lower panel of Figure 6, we have plotted the spectral parameters  $\Gamma_{\text{BAT}}$  and  $E_{\text{pt}}$ , along with the fluence in the BAT 15–150 keV range. The mean values of the spectral index  $\Gamma_{\text{BAT}}$  in the given energy range for SGRBs, LGRBs, bronze, silver, and gold subsamples, respectively, are  $-1.36 \pm 0.58$ ,  $-1.75 \pm 0.42$ ,  $-1.63 \pm 0.35$ ,  $-1.66 \pm 0.29$ ,  $-1.65 \pm 0.23$ , and  $-1.72 \pm 0.34$ . Since the BAT detects GRBs in the soft energy range (limited spectral coverage), the spectral peak energy of many bright GRBs can surpass this range. Due to this, some GRBs in the lower panel of Figure 6 show deviation from the distribution. We have calculated the mean values of the  $E_{\text{pt}}$  by removing the unphysical  $E_{\text{pt}}$  values, and the obtained mean values for SGRBs, LGRBs, bronze, silver, and gold samples, respectively, are  $99.93 \pm 70.48$ ,  $92.69 \pm 75.54$ ,  $111.54 \pm 84.096$ ,  $119.15 \pm 91.29$ , and  $75.41 \pm 53.16$  KeV. Our observations indicate that the gold and silver samples demonstrate a softer spectrum (though consistent within error bars) compared to the bronze subsample and LGRBs. At the same time, SGRBs exhibit the most hard spectral characteristics.

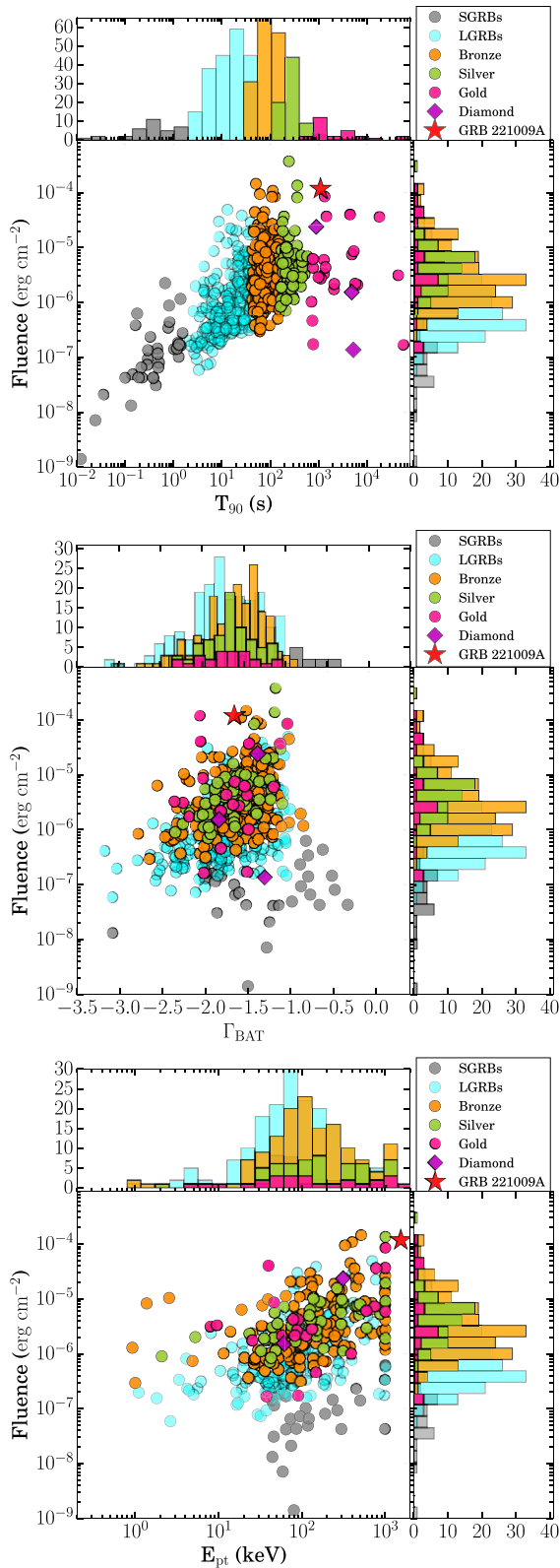


**Figure 6.** The upper panel represents fluence distribution in 15–150 keV, along with the durations of GRBs in our bronze, silver, gold, and diamond subsamples. The middle panel shows the spectral index ( $\Gamma_{\text{BAT}}$ ) obtained from fitting the time-integrated spectra of BAT with a power law, along with the fluence obtained in the 15–150 keV range. Similarly, the lower panel displays the distribution of  $E_{\text{pt}}$  along with the fluence obtained in the BAT energy range.

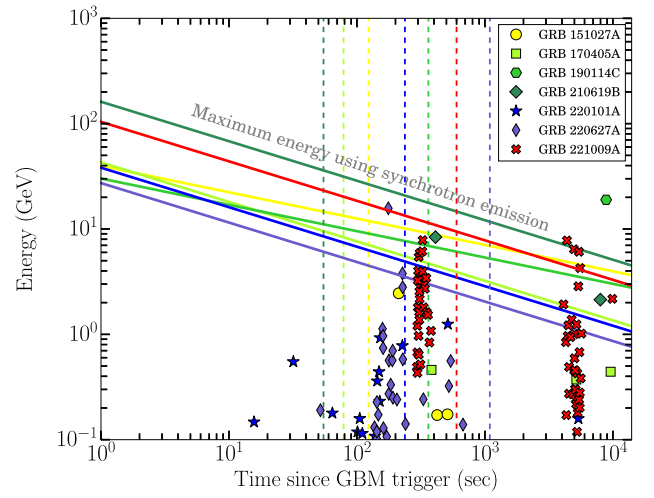


**Figure 7.** The Fermi-LAT observations of ULGRBs given in Table A7 with successful LAT detection. The various colored markers represent the photons with a probability of greater than 90% associated with these bursts. The corresponding colored lines represent the maximum limit allowed for synchrotron emission for each GRB. The vertical dashed lines show the end epoch of  $T_{90}$  prompt duration as observed by Fermi-GBM.

### 3.3. Search for GeV Emission Using Fermi-LAT Analysis

The duration of prompt emission (keV–MeV energy range) of ULGRBs is significantly longer, spanning 2–3 orders of magnitude compared to typical LGRBs (Levan et al. 2014). Nevertheless, owing to orbital constraints, Earth occultation, and limited sensitivity, it presents a challenge for instruments to capture all emissions throughout the entire duration of ULGRBs. To distinguish the high-energy emission (in the GeV energy range) of GRBs in the bronze, silver, and gold subsample from other bursts, we conducted an analysis of Fermi Large Area Telescope (LAT) data for GRBs that were simultaneously detected by both Swift-BAT and Fermi-GBM in our sample. We have listed the LAT boresight angle for these GRBs in Table A6. The analysis involved acquiring and examining LAT data using the `gtburst` software within a temporal range of 0–10 ks postdetection. A region of interest around the burst ( $10^\circ \times 10^\circ$ ) was defined while implementing a Zenith angle cut of  $100^\circ$  to reduce contamination from the Earth’s limb. The `P8R3_SOURCE` instrument response file was utilized for the analysis. The Fermi LAT time-integrated spectra within the 100 MeV–100 GeV range were fitted using a power-law model. To establish a detection threshold, the test statistic (TS) was used, setting  $\text{TS} > 15$  for adequate LAT detection. A more detailed method of Fermi LAT data analysis is presented in Gupta et al. (2021a). The likelihood of associating the photons with each burst is computed using the `gtsrcprob`. Following this analysis method, we found that there are three bronze (GRB 151027A Ruffini et al. 2018; GRB 170405A Arimoto et al. 2020; and GRB 210619B Caballero-García et al. 2023), two silver (GRB 190114C Fraija et al. 2019; GRB 220101A Mei et al. 2022), one gold (GRB 221009A, Lesage et al. 2023), and one diamond (GRB 220627A Y. -Y. Huang et al. 2022; de Wet et al. 2023) bursts in our sample with confirmed LAT detection (see Table A7). Figure 7 illustrates the number of high-energy photons detected with a probability greater than 90%, plotted

against time since the GBM trigger for all the seven bursts. In comparing LAT GeV light curves with the prompt emission duration of ULGRBs, the LAT emission persists beyond 10,000 s from the GBM trigger, indicating the presence of an extended high-energy emission for ULGRBs, typical to LGRBs. Furthermore, we also observe that, for a few GRBs, the origin of LAT emission is consistent with prompt keV–MeV emission (Y. -Y. Huang et al. 2022; de Wet et al. 2023; Lesage et al. 2023). This implies a shared internal region of emission encompassing the entire Fermi energy range for these bursts. However, the delayed and long GeV emission post prompt emission is expected to originate from the external shock model (Kumar & Barniol Duran 2009, 2010; Fraija et al. 2019; Caballero-García et al. 2023). Further, to explore the radiation mechanism of GeV LAT emission, we computed the maximum photon energy emitted by the synchrotron radiation mechanism in an adiabatic external forward shock during the decelerating phase, assuming an interstellar matter (ISM) or Wind stellar external medium following Piran & Nakar (2010) with number density values from literature (Fraija et al. 2019; Caballero-García et al. 2023; de Wet et al. 2023) or  $1 \text{ cm}^{-3}$ , if not available. It was observed that some late-time photons, with a source association probability exceeding 90%, surpass the maximum synchrotron energy for GRB 190114C, GRB 220627A, and GRB 221009A. This observation suggests a nonsynchrotron origin for these photons (Fraija et al. 2019; Lesage et al. 2023). In the case of recently detected VHE GRBs, photons above the maximum synchrotron energy point toward a Synchrotron self-Compton origin for these GeV photons (Abdalla et al. 2019; Collaboration et al. 2019; Fraija et al. 2019).

### 3.4. GRB 221009A in the Context of ULGRBs

ULGRBs, characterized by their exceptionally long prompt emission durations, are comparatively uncommon in comparison to typical LGRBs and SGRBs. However, the situation changes significantly when considering the initial variability in the X-ray light curve (Zhang et al. 2014). Some of the well-studied candidates of ULGRBs detected in the Swift era are listed in our gold and diamond subsamples given in Tables A1 and A2 and in Figure 8. It is worth noting that not all ULGRBs exhibit continuous emissions during the prompt phase, making it challenging to identify their ultralong nature. Moreover, the duration of a GRB depends on the sensitivity of the detecting instruments and orbital constraints. For example, GRB 091024A has a weak pulse at 0 s, followed by brighter emissions at  $\sim 600$  s and  $\sim 900$  s post burst, respectively. However, Swift-BAT detected only the first pulse (Virgili et al. 2013). On the other hand, GRB 220627A presents a double burst with the first pulse at 0 s and the second at 1000 s postburst, separated by a quiescent gap of around 600 s (de Wet et al. 2023). GRB 060218 (SN 2006aj; Campana et al. 2006) and GRB 100316D (SN 2010bh; Starling et al. 2011) exhibit soft and long prompt emissions lasting for 2100 and 1300 s, respectively, characteristics more akin to X-ray flashes than traditional GRBs. ULGRBs such as GRB 101225A (likely associated with an SN, Thöne et al. 2011), GRB 111209A (SN 2011kl; Greiner et al. 2015), GRB 130925A (Evans et al. 2014), GRB 141121A Cucchiara et al. (2015), and GRB 170714A Hou et al. (2018) have been observed during the prompt emission with extremely long durations and accompanied by a highly variable initial X-ray light curve. In contrast,

GRB 121027A (Peng et al. 2013), despite having a prompt duration of only 80 s, is classified as a ULGRB due to its highly variable X-ray Telescope (XRT) light curve, extending up to 2000 s. Subsequently, from the BAT survey data, the duration of GRB 121027A was derived as 5730 s (Lien et al. 2016), placing it in our gold subsample.

The prompt emission of GRB 221009A, as observed by Fermi-GBM, persisted above the background for more than 1000 s after the trigger, as depicted in the left panel of Figure A2. Notably, the prompt emission displayed a quiescent phase during which the central engine, although not entirely halted, produced multiple small pulses, maintaining the emission above the background levels. Lesage et al. (2023) demonstrated that, after 600 s, the GBM detection smoothly transitioned to the afterglow emission. GBM observed this afterglow emission for up to 1500 s before it was occulted by the Earth. Similarly, Konus-Wind recorded GRB 221009A for more than 600 s. Moreover, Konus-Wind identified a subsequent tail emission persisting for approximately 20 ks (Frederiks et al. 2023). In addition, authors have suggested that the duration of GRB 221009A is greater than 1000 s and discussed the possibility of this burst being a ULGRB (Burns et al. 2023). According to its reported  $T_{90}$  duration, GRB 221009A satisfies the criteria of being ULGRB given by Boër et al. (2015) ( $T_{90} > 1000$  s) and also belongs to our gold subsample.

However, no other low-energy X-ray or optical satellite was facing GRB 221009A to observe any soft flare during this time. Swift-BAT and XRT initiated an observation of GRB 221009A afterglow at 3300 s after  $T_0$ , with XRT light-curve decay with slope  $\alpha_x = 1.66 \pm 0.01$ . Figure 8 compares the temporal characteristics of GRB 221009A with those of other GRBs in our gold subsample. Except for the GBM (NaI-7, 9–900 keV) observation of GRB 221009A, all the light curves are plotted in the temporal range (10 s–100 ks) and energy range of 0.3–10 keV for BAT (black) and XRT (red). Figure 8 shows that most of the GRBs in our gold sample display either a plateau or flares during the early XRT light curve except for GRB 080319B and GRB 140614A, where a normal decay behavior can be seen throughout the afterglow phase. However, after 3300 s (time corresponding to the XRT trigger of GRB 221009A), the X-ray light curve for most of the GRBs decays following a simple power law, except for GRB 101225A, GRB 111209A, and GRB 170714A, where the plateau extends for more than 10 ks.

Our duration-based criteria place GRB 221009A in the gold subsample, indicating that GRB 221009A is likely a potential ULGRB candidate detected by Fermi and Swift missions. To provide a comprehensive perspective, the prompt emission characteristics of GRB 221009A have been compared with those of other GRBs, as well as with GRBs from our bronze, silver, gold, and diamond subsamples.

## 4. Possible Origin of Extended Duration in ULGRBs: Methodology and Tools

In this section, we examine the possible progenitor, central engine, environments, and other key characteristics of our subsamples using different methods (Bromberg et al. 2011; Li et al. 2018) and publicly available tools such as MESA. Our detailed methodology to constrain the possible progenitor and the central engine is described in Figure 1.

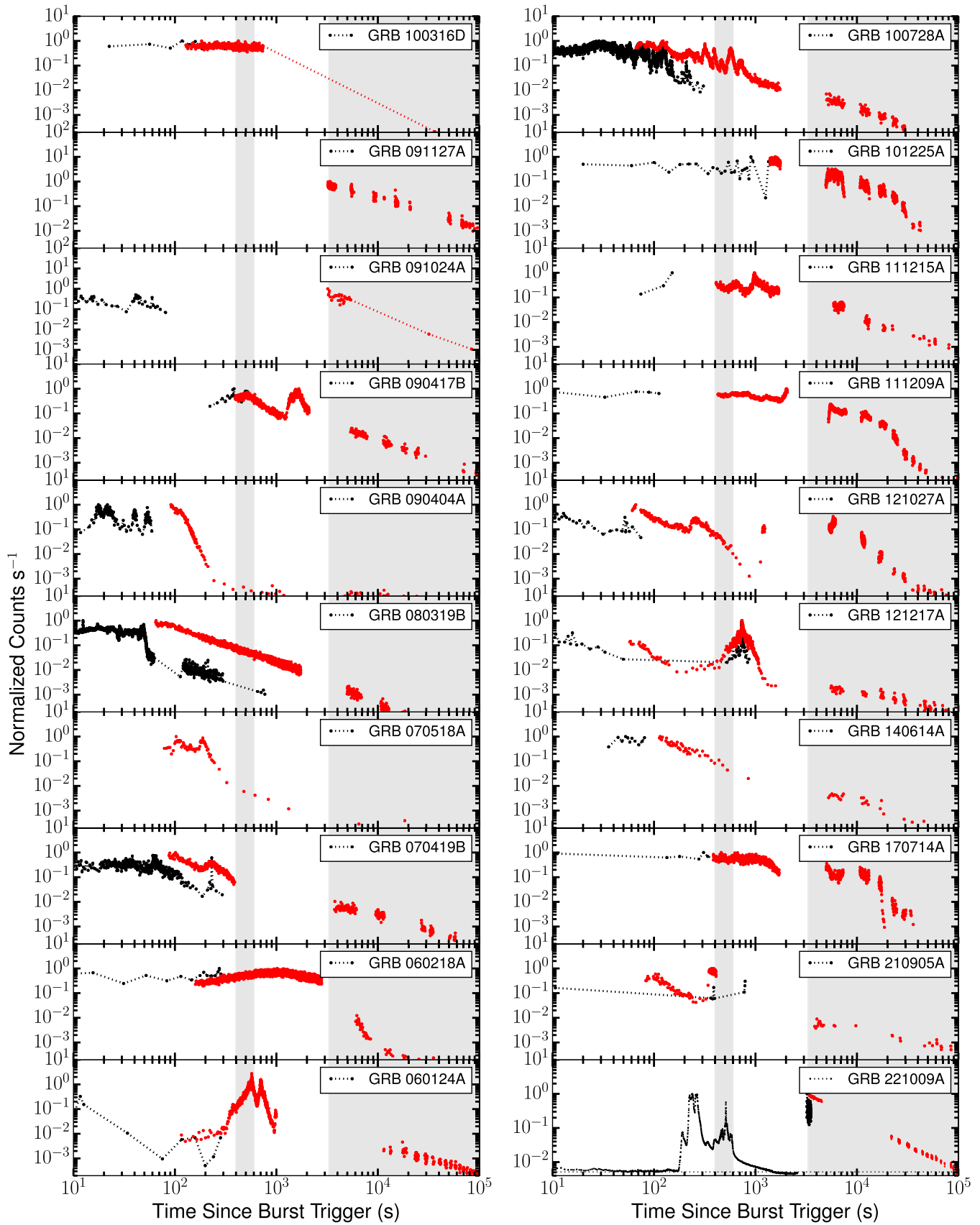


**Figure 8.** A comparison of GRB 221009A with the GRBs included in our gold subsample. The plot displays the normalized count-rate light curve observed by BAT and XRT in the 0.3–10 keV range. However, for GRB 221009A, the GBM observation in NaI-7 was utilized for prompt emission, while BAT and XRT were employed within the same 0.3–10 keV range. A thin shaded region at 500 s represents the GBM flash, and a wider one starting at 3300 s covers XRT observations of GRB 221009A.

#### 4.1. Supernova Connection with GRB 221009A?

The emerging SNe associated with nearby LGRBs are expected to cause a late red bump in the optical/near-IR (NIR) light curves and provide direct evidence of progenitors of GRBs (Galama et al. 1998; Hjorth et al. 2003). Previously studied nearby VHE-detected GRBs, including GRB 190114C, GRB 190829A, and GRB 201015A, as well as ULGRB GRB 111209A, have revealed similar late bumps. These features are indicative of their associated SNe and potential progenitor systems (Campana et al. 2006; Starling et al. 2011; Greiner et al. 2015). Both the close proximity and the long duration of GRB 221009A indicate the potential presence of a late optical bump in the afterglow light curve. Early spectroscopic observations taken using the 10.4 m Gran Telescopio Canarias (de Ugarte Postigo et al. 2022) and subsequent photometric investigations (Fulton et al. 2023) suggested the presence of an underlying SN (initially dubbed SN 2022ixw) associated with GRB 221009A. However, findings from A. J. Levan et al. (2023), Laskar et al. (2023), and Shrestha et al. (2023) neither support nor refute the presence of the underlying SN emission associated with GRB 221009A. Further, the late-time ( $\sim T_0 + 170$  days) spectroscopic observation by the James Webb Space Telescope also favors the underlying SN with observed spectral features similar to SN 1998bw (Blanchard et al. 2024). Figure 9 illustrates the light curve of GRB 221009A obtained using our NIR observations along with data reported in the General Coordinates Network (GCN) and R. Sánchez-Ramírez et al. (2024, in preparation). Our observations revealed a consistent, smooth decay in the NIR light curve of GRB 221009A, distinct from the presence of bumps or flattening features as observed in the background light curves of SN-connected GRBs. Hence, our NIR observations do not provide evidence for the presence of any bright SN connected with GRB 221009A. However, faint SN emission may be masked by the bright afterglow emission of GRB 221009A.

#### 4.2. Constraining the Possible Progenitor: Collapsar Origin?

Recent discoveries of GRB 200826A, GRB 211211A, and GRB 230307A have challenged our perception of the relation between  $T_{90}$  and the origin of GRBs. GRB 200826A (Ahumada et al. 2021) identified as an SGRB with a duration ( $T_{90}$ ) of 1.14 s, accompanied by an underlying SN. Additionally, GRB 211211A (Troja et al. 2022) and GRB 230307A (A. Levan et al. 2024), with a duration of 50 and 35 s, respectively, are LGRBs originating from compact binary mergers.

In this section, we determine the origin (collapsar or merger) of the bursts in our bronze, silver, and gold subsamples following Bromberg et al. (2011) and determine their noncollapsar probability. The duration of the prompt emission of GRBs, represented by  $T_{90}$  value, cannot be shorter than the time the engine remains active after the jet breakout. In most GRB models, these two durations are considered equal, denoted as  $T_{90} = T_{\text{Eng}} - t_b$ , where  $T_{\text{Eng}}$  is the duration for which engine is active, and  $t_b$  is the time taken by the jet to come out of the preexisting envelope surrounding the progenitor star. It is unlikely that the engine will operate precisely long enough for the jet to break out of the star and then cease immediately afterward. This condition directly stems from the Collapsar model, implying that if ULGRBs originate from Collapsars, they must adhere to this criterion. To

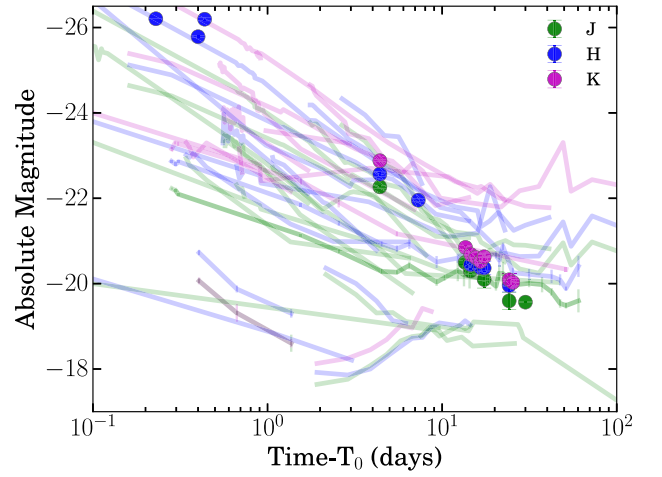


**Figure 9.** The light curve of GRB 221009A in NIR bands (*J*, *H*, and *K*) is shown in colored circles. The data utilized for this plot are obtained from observations made with the 3.6 m DOT (Gupta et al. 2024); see also Pandey (2016, 2018), published GCNs, and R. Sánchez-Ramírez et al. (2024, in preparation). Other GRBs connected to supernovae are also shown with colored lines in the background. The GRBs shown and corresponding references are: GRB 011121 (Price et al. 2002; Garnavich et al. 2003), GRB 030329A (Bloom et al. 2004), GRB 060218A (Kocevski et al. 2007), GRB 071112A (Klose et al. 2019), GRB 081007A (Jin et al. 2013), GRB 091127A (Olivares et al. 2015), GRB 101219A (Olivares et al. 2015), GRB 111228A (Klose et al. 2019), GRB 111209A (Kann et al. 2018), GRB 120422A (Schulze et al. 2014), GRB 130215A (Cano et al. 2014), GRB 130427A (Perley et al. 2014), GRB 130702A (Toy et al. 2016), GRB 130831A (Klose et al. 2019), GRB 161219B (Cano et al. 2017), GRB 190114C (Collaboration et al. 2019; Gupta et al. 2021b), GRB 190829A (Hu et al. 2021).

know the origin of GRBs in our sample, we calculated the jet opening angle ( $\theta_j$ ), which is then used to calculate  $t_b$ . Then, we calculated the ratio  $T_{90,z}/t_b$  to constrain the possible progenitor of bronze, silver, and gold subsamples. We have used the following relation provided in Bromberg et al. (2011) to calculate  $t_b$ :

$$t_b(\text{s}) \sim 15 \epsilon_\gamma^{1/3} L_{\gamma,\text{iso},50}^{-1/3} \theta_{j,10^\circ}^{2/3} R_{11}^{2/3} M_{15\odot}^{1/3}. \quad (1)$$

In this equation,  $L_{\gamma,\text{iso},50} = \frac{L_{\gamma,\text{iso}}}{10^{50}} \text{ erg s}^{-1}$ , where  $L_{\gamma,\text{iso}}$  is the gamma-ray luminosity at the peak of the prompt light curve.  $\theta_{j,10^\circ} = \theta_j/10^\circ$ , where  $\theta_j$  is jet opening angle.  $R_{11} = R/10^{11} \text{ cm}$ , and  $M_{15\odot} = M/15 M_\odot$ , where  $R$  and  $M$  are the radius and the mass of the star, respectively. The calculated values of  $L_{\gamma,\text{iso},50}$  for each burst included in our sample are given in Table A1.  $\epsilon_\gamma$  is the radiative efficiency, fixed at 0.1 (Bromberg et al. 2011). We calculated  $\theta_j$  using Equation (4) of Sharma et al. (2021). For the GRBs in our sample with clear evidence of a jet break, based on temporal and spectral indices, the time corresponding to the jet break ( $t_j$ ) is taken directly from the Swift-XRT webpage<sup>13</sup>; otherwise, the last data point in the Swift-XRT light curve is assumed to be  $t_j$ , providing a lower limit on  $\theta_j$ . Initially, the mass ( $M$ ) of the progenitor star is varied from  $15 M_\odot$  to  $30 M_\odot$ , and the radius ( $R$ ) is also accordingly varied.

In this section, we initially determine the effect of mass and radius on  $t_b$ . We note that, changing the mass from 15 to  $30 M_\odot$  and keeping the radius fixed at  $10^{11} \text{ cm}$ , there is only 20% decrement in ratio  $T_{90,z}/t_b$  utilizing Equation (1). Further, we vary the radius of star using the relation  $R = 1.33M^{0.55}$  given by Demircan & Kahraman (1991) when the mass is changed from 15 to  $30 M_\odot$ . Thus, utilizing Equation (1), once again, we

<sup>13</sup> [https://www.swift.ac.uk/xrt\\_live\\_cat/](https://www.swift.ac.uk/xrt_live_cat/)

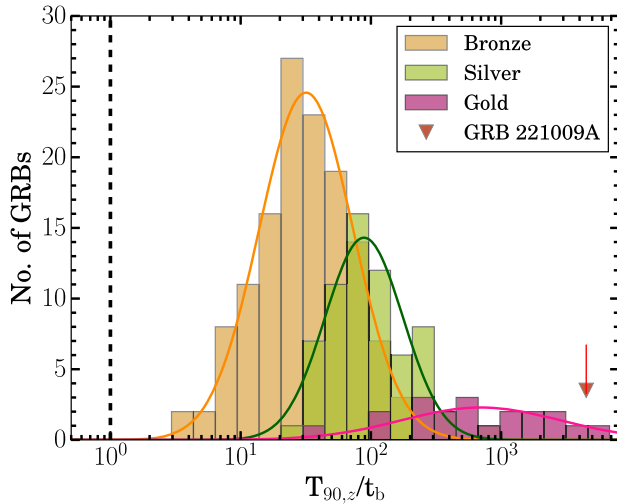


**Figure 10.** Distribution of the ratio of the rest frame  $T_{90,z}$  and  $t_b$  calculated for bronze, silver, and gold samples. The vertical dashed line indicates the rest frame  $T_{90} = t_b$ .

estimate corresponding  $T_{90,z}/t_b$ ; we find that, when both mass and radius are varied, there is a decrement of 38% in ratio  $T_{90,z}/t_b$ . We have shown the above calculation in Section A.3.

Hence, there is no significant effect of  $M$  and  $R$  of the progenitor star in the calculation of  $T_{90,z}/t_b$  values in the considered range of mass and radius. Finally, we have used the progenitor star’s mass and radius equal to  $15M_{\odot}$  and  $10^{11}$  cm, respectively (Bromberg et al. 2011). The results of the distribution of  $T_{90,z}/t_b$  calculated for our bronze, silver, and gold subsamples are given in Figure 10 and Table A1. The vertical black dashed line in the plot indicates  $T_{90} = t_b$ , and all GRBs left of this line are considered to be of noncollapsar origin (Bromberg et al. 2011). We noted that all GRBs in our sample lie to the right of the black dashed line, consistent with the collapsar origin. In addition, we have determined the probability of noncollapsar origin for our sample of GRBs by using Equations (1) and (2) from Bromberg et al. (2013). The probability values obtained are listed in Table A1. Negligible values of noncollapsar probabilities indicate the collapsar origin of the GRBs included in our bronze, silver, and gold subsamples.

#### 4.3. Constraining the Central Engine

Even after more than 50 yr of GRB discovery, there is still much to learn about the central engines of GRBs. In this section, we constrain the possible central engines of our bronze, silver, and gold subsamples following the methodology presented in Li et al. (2018) and Sharma et al. (2021).

In the context of the compactness problem and the highly variable prompt emission light curve, a rapidly rotating compact object with an accretion disk is essential as a central engine for GRBs. Generally, two types of central engines are considered: a hyperaccreting black hole and a millisecond magnetar. While there is no direct observational evidence confirming the nature of the inner compact objects, certain features observed in the afterglow light curve provide some clues regarding their nature. A black hole central engine is the most important candidate for explaining the observed energy of GRBs. The power of a jet originating from a hyperaccreting black hole stems from two primary energy sources. First, the accretion energy present in the disk gives rise to neutrinos and

antineutrinos. These particles annihilate each other, generating a collimated outflow (Qian & Woosley 1996). Second, the rotational energy possessed by a Kerr black hole can be harnessed using magnetic fields through the process known as the Blandford–Znajek mechanism proposed by Blandford & Znajek (1977). The energy released during the spin-down of a magnetar can also play a significant role in the formation of a bipolar jet (Bucciantini et al. 2007, 2009). However, the magnetar central engine relies on the fundamental concept that the maximum achievable rotational energy, approximately of the order of  $10^{52}$  erg, is possible to power jets from a millisecond magnetar. It is noteworthy that such a limit does not apply to a black hole central engine. Therefore, in this study, we leverage the maximum achievable rotational energy of a magnetar to investigate the potential central engine of GRBs. The rotational energy of a millisecond magnetar can be expressed as  $E_{\text{rot}} = \frac{1}{2}I\Omega^2$ , where  $I$  represent the moment of inertia of the magnetar with mass  $M_m$  and radius  $R_m$ . The moment of inertia of a solid sphere is given by  $I = \frac{2}{5}MR^2$ . The angular velocity  $\Omega$  related to the period  $P_m$  by the formula  $\Omega = 2\pi/P_m$ . Considering the parameters  $M_m = 1.4M_{\odot}$ ,  $R_m = 10$  km, and  $P_m = 1$  ms as discussed in Lü & Zhang (2014), the calculated value of rotational energy  $E_{\text{rot}}$  is approximately  $2.2 \times 10^{52}$  erg, which closely aligns with the value assumed for our analysis.

For those GRBs in our sample simultaneously detected by Fermi-GBM and Swift-BAT (there are 32 such GRBs), we independently calculated the  $E_{\gamma,\text{iso}}$  using Fermi-GBM observations. For these GRBs, we have retrieved Fermi-GBM data from the official Fermi webpage.<sup>14</sup> Then, the time-integrated spectra for these GRBs are reduced by utilizing the latest version of the `gtburst` software. Furthermore, the Multi-Mission Maximum Likelihood 3ML (Vianello et al. 2015) framework is used for the spectral fitting of these time-integrated spectra. We fitted the Band function to each spectrum, and the spectral parameters obtained are given in Table A6. The flux was calculated for each GRB in the energy range  $10/(1+z)$  to  $10,000/(1+z)$ , and using these values, we determined the isotropic gamma-ray energies  $E_{\gamma,\text{iso}}$  for each burst in the sample. Furthermore, we calculated the beaming corrected gamma-ray energy  $E_{\theta,\gamma,\text{iso}} = f_b \times E_{\gamma,\text{iso}}$ , where  $f_b = 1 - \cos(\theta_j) \sim 1/2(\theta_j)^2$  is the beaming correction factor. If the beaming corrected energy is greater than the maximum energy budget of a magnetar (i.e.,  $E_{\theta,\gamma,\text{iso}} > 2 \times 10^{52}$ ), it rules out the possibility of a magnetar central engine (Sharma et al. 2021). The histogram distributions of  $E_{\gamma,\text{iso}}$  and  $E_{\theta,\gamma,\text{iso}}$  for Fermi-GBM detected bursts are shown in left and middle panels of Figure 11. We found only two GRBs (GRB 210619B and GRB 221009A) having  $E_{\theta,\gamma,\text{iso}} > 2 \times 10^{52}$  erg for which a magnetar is excluded, while a black hole could be the possible central engine. For these cases, we have constrained the mass of the black hole using Equations (5)–(7) of Sharma et al. (2021) and obtained the black hole masses  $\sim 3.4M_{\odot}$  and  $\sim 9.1M_{\odot}$ , respectively, for GRB 210619B and GRB 221009A.

For those GRBs in our sample only detected using Swift-BAT, we searched for the plateau in the Swift-XRT light curve and found 74 out of 230 GRBs exhibited at least one plateau. We retrieved the Swift-XRT spectra during the plateau phase and performed the spectral fitting. The methodology of Swift-XRT spectral fitting used to fit individual spectrum is given in

<sup>14</sup> <https://heasarc.gsfc.nasa.gov/W3Browse/fermi/fermigbrst.html>

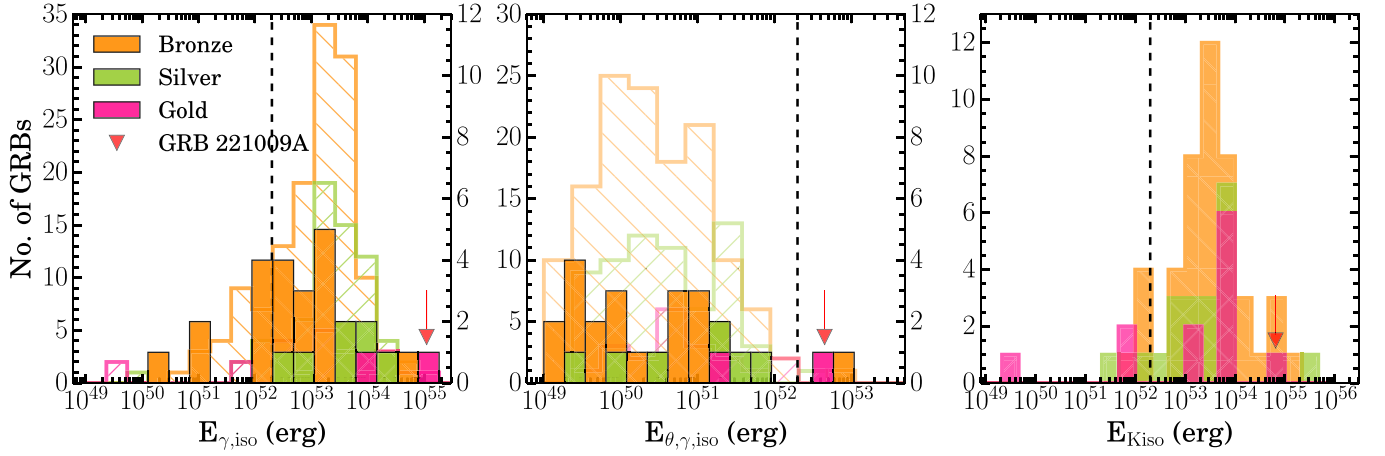


**Figure 11.** Histogram distribution of the isotropic energy ( $E_{\gamma, \text{iso}}$ ) (left), beaming corrected isotropic energy ( $E_{\theta, \gamma, \text{iso}}$ ) (middle) of Fermi (solid) and Swift (empty) detected bursts. Right: kinetic energy ( $E_{K, \text{iso}}$ ) of Swift-detected bursts. Black dashed lines at  $2 \times 10^{52}$  erg represent the maximum energy budget of a magnetar central engine.

the Appendix A.2. For these bursts, we have calculated the isotropic X-ray energy ( $E_{X, \text{iso}}$ ) corresponding to the plateau phase, total isotropic gamma-ray energy ( $E_{\gamma, \text{iso}}$ ), and the kinetic energy ( $E_{K, \text{iso}}$ ) to constrain the possible central engine of these Swift only detected burst. We have calculated  $E_{X, \text{iso}}$  released during the plateau phase using the following relation:

$$E_{X, \text{iso}} = \frac{4\pi k D_L^2}{1+z} \times F_X, \quad (2)$$

where  $D_L$  is the luminosity distance, and  $F_X$  is X-ray fluence in the Swift-XRT energy range.  $k = (1+z)^{(\beta_X-1)}$ , where  $\beta_X$  is the spectral index obtained from the X-ray spectral fitting, and  $z$  is the redshift. Further, we have calculated  $E_{K, \text{iso}}$  of these GRBs using the relations given in Zhang et al. (2007).  $E_{K, \text{iso}}$  of any GRB depends on the spectral regime and profile of the circumburst medium. We have considered the slow cooling regime. Even if the observed spectrum initially falls into the fast cooling regime (i.e.,  $\nu_m > \nu_c$ ), it is crucial to note that the evolution of  $\nu_m (\propto t^{-3/2})$  is faster than the  $\nu_c (\propto t^{-1/2}$  for ISM or  $t^{1/2}$  for Wind-like medium). Consequently,  $\nu_m$  rapidly crosses  $\nu_c$ , resulting in the observed spectral shape predominantly lying within the slow cooling regime. Moreover, the X-ray afterglow modeling results presented by Beniamini et al. (2015) indicate that the X-ray emitting electrons typically lie in the slow cooling regime. Given these considerations, it is indeed relevant to consider the slow cooling regime in our analysis.

Based on the ISM or Wind-like surrounding medium and the location of break frequencies, the following three cases are possible:

- (1) For the spectral regime  $\nu_x > (\nu_m, \nu_c)$ , the spectral indices are independent of the profile of the circumburst medium; we have used Equation (8) of Li et al. (2018) to calculate  $E_{K, \text{iso}}$ .
- (2) For  $\nu_x < \nu_c$  spectral regime and Wind-like surrounding media, the relation for  $E_{K, \text{iso}}$  is given by Equations (10) of Li et al. (2018).
- (3) For  $\nu_x < \nu_c$  spectral regime and ISM-like surrounding media, Equation (11) from Li et al. (2018) is utilized to determine ( $E_{K, \text{iso}}$ ). In these equations,  $\nu F_\nu (\nu = 10^{18})$  is the energy flux at  $10^{18}$  Hz.  $\epsilon_e$  (fixed at 0.1) and  $\epsilon_B$  (fixed at 0.01) are the efficiencies of energy transfer to the

electrons and magnetic field, respectively.  $Y$  (fixed at 1) is the Compton parameter. The density parameter  $n = 1$  is taken for an ISM-like surrounding medium, and  $A_*$  is the density parameter for a Wind-like surrounding medium. Initially, we used the closure relations by utilizing the temporal and spectral indices of the normal decay phase followed by the plateau phase of X-ray afterglow to constrain the spectral regime and the surrounding medium profile for each GRB. For the corresponding best possible spectral regime and the surrounding medium of each GRB, we calculated  $E_{K, \text{iso}}$  values. The histogram distribution of  $E_{K, \text{iso}}$  is shown in the right panel of Figure 11. The calculated values of  $E_{X, \text{iso}}$  and  $E_{K, \text{iso}}$  are listed in Table A1.

The distributions of  $E_{X, \text{iso}}$  as a function of  $E_{K, \text{iso}}$ , and  $E_{\gamma, \text{iso}}$  for our sample are shown in the upper and lower panels of Figure 12, respectively. The distribution of  $E_{K, \text{iso}}$  versus  $E_{X, \text{iso}}$  shows that three GRBs (GRB 110213A, GRB 121027A, and GRB 140206A) have both  $E_{K, \text{iso}} > 2 \times 10^{52}$  erg and  $E_{X, \text{iso}} > 2 \times 10^{52}$  erg, supporting the black hole as a possible central engine for these GRBs (Li et al. 2018). Additionally, GRB 060218A, GRB 100316D, GRB 110808A, GRB 150915A, GRB 161108A, GRB 171205A, and GRB 180329B have both  $E_{K, \text{iso}} < 2 \times 10^{52}$  erg and  $E_{X, \text{iso}} < 2 \times 10^{52}$  erg; for these GRBs, a magnetar central engine is preferred. For the rest of the bursts of our sample,  $E_{K, \text{iso}} > 2 \times 10^{52}$  erg and  $E_{X, \text{iso}} < 2 \times 10^{52}$  erg, a black hole central engine is poorly constrained (Li et al. 2018). GRB 221009A does not have a plateau in the observed XRT light curve; considering the possibility of an early plateau, we calculated the lower limit of  $E_{X, \text{iso}}$  utilizing the first XRT data point (see Figure 12). The calculated lower limit also favors a black hole central engine for GRB 221009A. Further, we have also studied the distribution of  $E_{X, \text{iso}}$  as a function of  $E_{\gamma, \text{iso}}$  for our sample (see the lower panel of Figure 12). We calculated  $E_{X, \text{iso}}$  only during the plateau phase instead of the complete duration of X-ray afterglow and found a positive correlation (Lan et al. 2023). We calculated the Pearson correlation and found a positive correlation with  $r = 0.73$  and a  $p$ -value of  $< 10^{-4}$ . We found a linear relation as  $\log(E_{\gamma, \text{iso}}) = (0.77 \pm 0.05) \times E_{X, \text{iso}} + 13.45 \pm 2.08$ . We have also shown the data points given in Li et al. (2018) along with our sample.

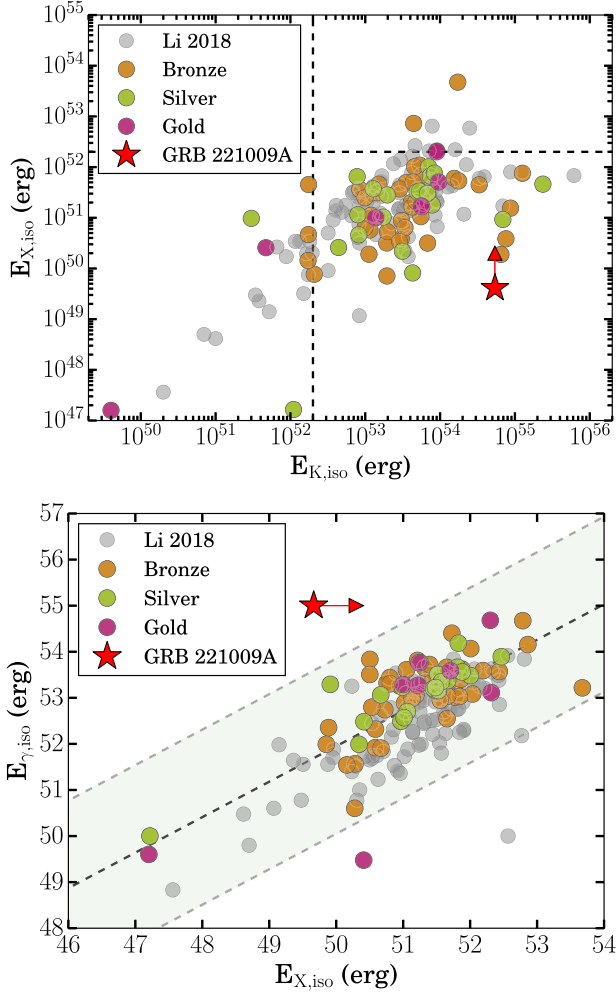


**Figure 12.** Upper panel: distribution of  $E_{X,iso}$  vs.  $E_{K,iso}$  calculated for GRBs with plateau in the XRT light curve in our bronze, silver, and gold subsamples. Similarly, gray circles represent the GRBs taken from Li et al. (2018). Black dashed lines at  $2 \times 10^{52}$  erg represent the maximum energy budget of a magnetar central engine. Lower panel: distribution of  $E_{X,iso}$  vs.  $E_{\gamma,iso}$ , the dashed lines represent the power law fitted to the distribution along with  $1\sigma$  uncertainty. GRB 221009A, as shown with a red star, does not have a plateau. The obtained lower limit of  $E_{X,iso}$  is calculated from the first data point of Swift-XRT observation.

#### 4.4. Environment of ULGRBs

Evans et al. (2014) suggested that ULGRBs may be distinguished from LGRBs due to their unique circumburst environment instead of different progenitor systems. The authors also proposed that ULGRBs occur in environments with extremely low densities, which can cause their ejecta to decelerate more slowly than they would in denser environments. To study the environmental properties of our sample, we used the intrinsic X-ray absorbing column density ( $N_{H,z}$ ) as a parameter to estimate the amount of absorbing material along the line of sight, utilizing Swift-XRT data. The intrinsic column densities around a burst were calculated by fitting the X-ray afterglow spectra using XSPEC software (Arnaud 1996). We obtained our results by selecting a spectrum corresponding to the late time of the XRT light curve. This is particularly important because any early variation in the X-ray spectrum, such as a steep decay phase or flare, would reverberate the column density value and produce biased values (Dalton &

Morris 2020). Each spectrum is then fitted by a power law including the absorption components  $zphabs$  and  $phabs$ , respectively, due to the Galactic ( $N_{H,Gal}$ , fixed) and intrinsic host ( $N_{H,z}$ ) at the redshift of the GRBs. The  $N_{H,z}$  distribution for our subsamples as a function of redshift is shown in Figure 13. The mean values of  $N_{H,z}$  for bronze, silver, and gold subsamples are  $2.90 \times 10^{22}$ ,  $1.83 \times 10^{22}$ , and  $1.25 \times 10^{22} \text{ cm}^{-2}$ , respectively. Further, we check if there is any dependence of  $N_{H,z}$  on redshift. There is an increasing trend of  $N_{H,z}$  with redshift, as observed in the previous works (Campana et al. 2010). Although obtained from different methods,  $N_{H,z}$  evolution with redshift in Figure (1) of Tanvir et al. (2019) is nearly flat. Similarly, we conducted a comparative analysis of the optical host extinction ( $A_{V,host}$ ) at the locations of GRBs within our gold, silver, and bronze subsamples along with GRBs given in Kann et al. (2010), Schady et al. (2010), de Ugarte Postigo et al. (2011), Wang & Dai (2014), Lyman et al. (2017), Zafar et al. (2018), Nugent et al. (2022), and Schroeder & Laskar (2022). The lower panel of Figure 13 illustrates that GRBs in SGRBs, LGRBs, bronze, silver, and gold subsamples display extinction characteristics consistent with each other. Four GRBs in the gold subsample show a high value of  $A_{V,host}$ , possibly due to the dark nature of these bursts (Holland et al. 2010; Xin et al. 2010; van der Horst et al. 2015). However, the limited number of GRBs with measured host extinction properties in our sample poses a challenge in drawing definitive conclusions.

### 5. Constraints on the ULGRB Progenitors Using MESA Simulation

Late-time ( $>1$  day) afterglow observations of low-redshift LGRBs have revealed that these events are sometimes accompanied by a special type of broad-line SNe-Ic (Galama et al. 1998; Hjorth et al. 2003; Kumar et al. 2022), indicating the collapsar origin of LGRBs (Woosley 1993). SNe-Ic shows no H and He lines in their spectral signatures, indicating extensive mixing of elements or violent mass loss in their progenitor stars. Simulations have shown that rapidly rotating massive stars with enhanced mixing rates can undergo quasicompositional evolution (Yoon & Langer 2005; Yoon et al. 2006). Enhanced mixing ensures most of the H and He take part in the combustion due to the transport of these elements from the envelope to the core. The remaining H in the envelope can be removed by rotation-driven wind (Yoon & Langer 2005; Yoon et al. 2006; Aguilera-Dena et al. 2018) that leads to the W-R star as the final stage, which could be the progenitors of LGRBs. The progenitor of ULGRBs requires an additional condition: the freefall time of the envelope must be enough to feed the jet for a longer timescale than for typical LGRBs (Perna et al. 2018). There is significant interest in studying the evolution of massive stars that match the characteristics of ULGRB progenitors.

The prolonged duration of ULGRBs in comparison to LGRBs suggests a distinct origin. In Section 4.2, our analysis rules out compact object mergers as the possible progenitor of ULGRBs and favors the collapsar scenario (Galama et al. 1998; Hjorth et al. 2003), similar to typical LGRBs (while certain LGRBs, such as GRB 211211A and GRB 230307A, have been identified as originating from compact object mergers). Moreover, the environment and prompt emission spectral properties of GRBs in our sample are consistent with those of typical LGRBs (see Figures 6, 13, and A3), implying similarities in jet

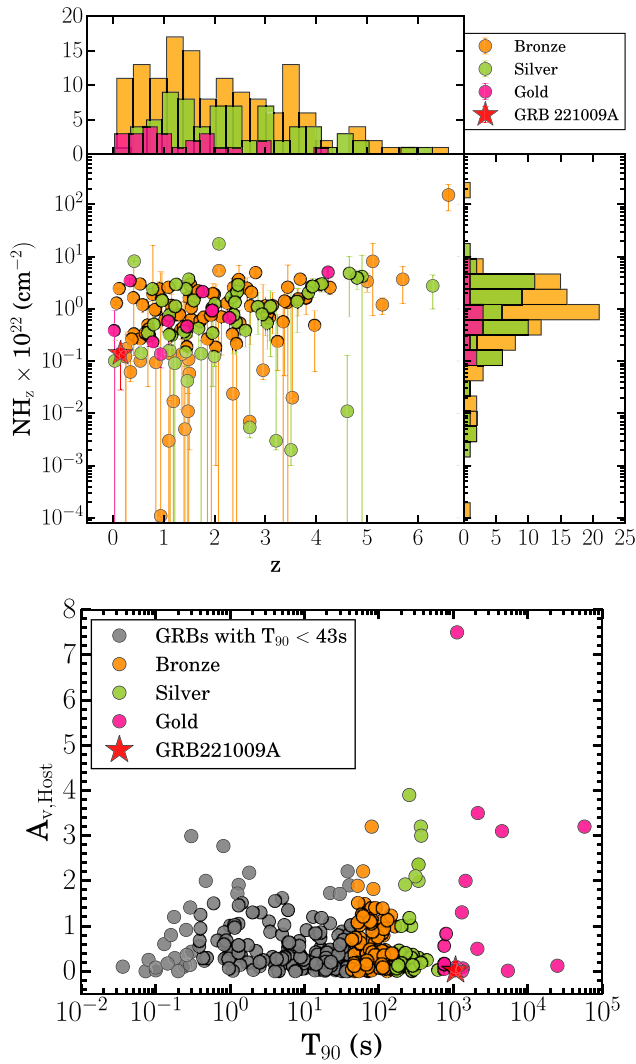


**Figure 13.** Upper panel: represents the distribution of intrinsic X-ray column density ( $NH_z$ ) for our bronze, silver, and gold subsample as a function of redshift. Lower panel: displaying the host extinction in the V band ( $A_{v,host}$ ) at the redshifts of the bronze (orange), silver (green), and gold/ULGRBs (red) subsamples, alongside additional GRBs (gray) documented in Kann et al. (2010), Schady et al. (2010), Perley et al. (2013), Wang & Dai (2014), Lyman et al. (2017), Zafar et al. (2018), Nugent et al. (2022), Schroeder et al. (2022), and Levan et al. (2023).

composition and emission processes associated with ULGRBs and LGRBs, respectively. Therefore, it becomes important to distinguish the type of collapsing massive stars that can fuel the central engine 100–1000 times longer than collapsing typical W-R stars for LGRBs (Woosley 1993). It is assumed that, due to the larger radius of BSG stars than W-R stars, freely falling outer envelopes take a longer time and, in turn, provide accretion for a longer duration to keep the central engine active to produce ULGRBs (Perna et al. 2018). Larger radii significantly increase the freefall time of the accreting material to the central engine or the active time for the central engine ( $T_{\text{Engine}}$ ). Consequently,  $T_{90} = T_{\text{Engine}} - t_b$  for the massive stellar object ( $15\text{--}30 M_{\odot}$ ) can sufficiently account for the observed duration of ULGRBs. In addition, SN 2011kl associated with ULGRB 111209A differs from typical type Ic SNe (Greiner et al. 2015) although the spectrum lacks H and He; it shows very little metal abundance. However, the missing

H/He in the spectra of SNe associated with ULGRBs can also be due to the ionization of the ejecta due to the high-energy emission from the central engine (Ioka et al. 2016).

Our analysis in Section 4.2 indicates that, upon increasing mass within the selected mass range ( $15\text{--}30 M_{\odot}$ ), there is marginal change in the jet bore-time  $t_b$  if the final collapsing star is a W-R or BSG. This implies the GRB jet can bore through the W-R and BSG stars. However, if the collapsing star is in the red supergiant (RSG) phase, the radius of the star could be several  $100\text{--}1000 R_{\odot}$ ; in such a case, jet bore-time could be very high ( $\gtrsim 100$  s), and the emergence of the jet cannot be possible through these stars. Such an effect of larger precollapse radii of RSGs has been also observed by Perna et al. (2018). These results indicate that the W-R and BSG stars could be the progenitors of LGRBs, and the equation for the estimation of  $t_b$  is properly useful only for W-R and BSG progenitors.

### 5.1. Evolution of Massive Star with MESA

After studying the detailed prompt and afterglow properties of a number of ULGRBs in previous sections, we have performed the simulation of massive stars with different initial masses and rotations utilizing the state-of-the-art tool, MESA, to refine our understanding of their progenitor. In this subsection, we provide the details of the 1D stellar evolution of possible progenitor models using MESA. Beginning from their pre-main-sequence (PMS) stages, the models evolve up to the stage of the onset of core collapse. Considering various characteristics of the possible progenitors outlined in the previous studies (Aguilera-Dena et al. 2018; Perna et al. 2018; Song & Liu 2023), we have chosen the initial conditions to simulate the evolution of massive stars. We obtain the final physical properties, including the radius, surface temperature, and luminosity of the collapsing stars, from MESA as they enter the core-collapse phase. These parameters are then used to constrain the freefall time of the collapsing star models. Further, we compare the derived freefall time with the observed  $T_{90}$  duration of both LGRBs and ULGRBs, aiding in the understanding of the physical characteristics of stars capable of producing such GRBs.

In our study, to simulate the evolution of massive stars starting from the PMS until they reach the stage of the onset of core collapse, we employ MESA version 23.05.1. Our primary objective is to utilize the final parameters of these massive stars at the stage of the onset of core collapse to estimate whether they can allow the formation and successful penetration of jets from the surrounding envelope to produce a GRB. Finally, we estimate the freefall time ( $t_{ff}$ ) to gain insights into how long the central engine can be fueled, which helps us to distinguish between LGRBs and ULGRBs (Perna et al. 2018). The variety of MESA parameters in this study to evolve our models up to the stage on the onset of core collapse closely follows the MESA settings of Aryan et al. (2021) and Aryan et al. (2022). However, we discuss a few changes ahead. The stellar models in our study have zero age main-sequence (ZAMS) masses of 15, 20, 25, and  $30 M_{\odot}$ . Starting from the initial angular rotational velocity ( $\Omega$ ) of  $0.1 \Omega_c$ , the  $\Omega$  for each model is varied up to  $0.6 \Omega_c$ , where  $\Omega_c$  is the critical angular rotational velocity and is expressed as  $\Omega_c^2 = (1 - L/L_{\text{edd}})GM/R^3$ , with  $L_{\text{edd}}$  representing the Eddington luminosity. Further, for each model, we employ a metallicity ( $Z$ ) of  $2 \times 10^{-4}$ , which is

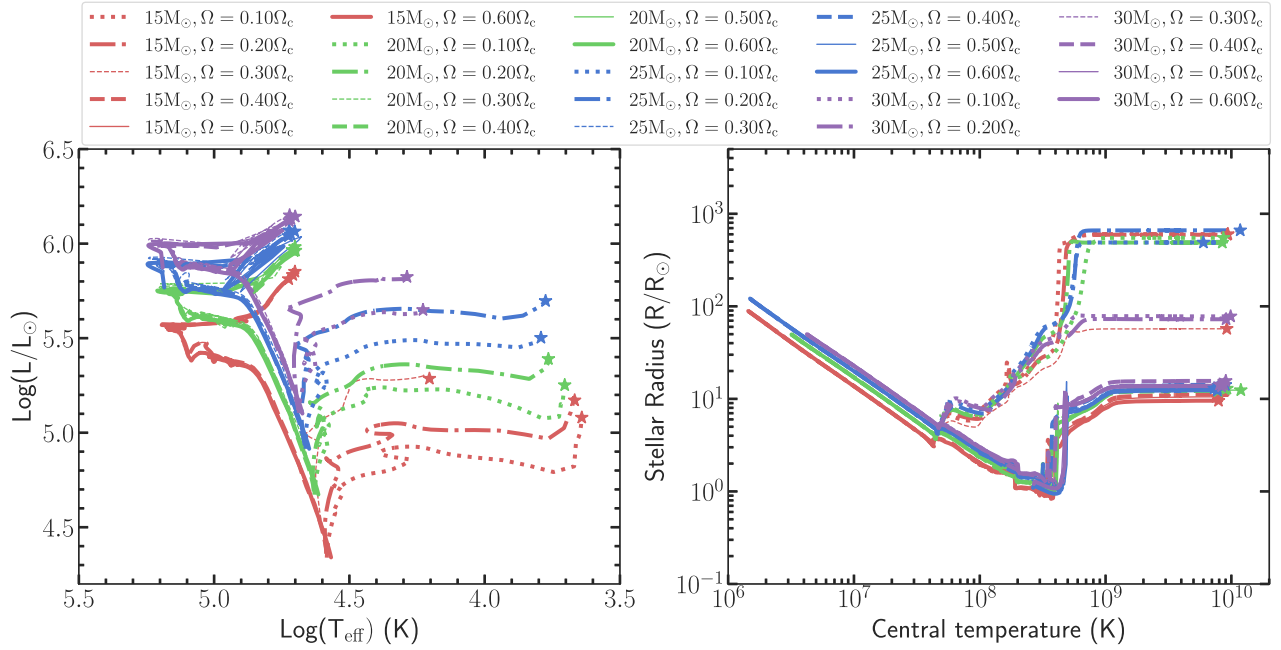


**Figure 14.** Left: The evolution of our models having ZAMS masses of 15, 20, 25, and 30  $M_{\odot}$  on the H-R diagram. For each model having a particular ZAMS mass, the initial rotation is varied in steps of 0.1  $\Omega_c$  up to 0.6  $\Omega_c$ . Right: The evolution of the stellar radius vs. central temperature curve of each model as the model progresses on the H-R diagram. The stage of the onset of core collapse for each model is marked by  $\star$ .

avored by host galaxy observations of LGRBs (Le Floc’h et al. 2003; Mannucci et al. 2011; Gupta et al. 2022c).

We adopt the Ledoux criterion and model the convection utilizing the mixing length theory of Henyey et al. (1965) by fixing the mixing length parameter ( $\alpha_{\text{MLT}}$ ) to 2.0. The semiconvection coefficient  $\alpha_{\text{sc}}$  is fixed to 0.01 to introduce the effect of semiconvection by following Langer et al. (1985). The thermohaline mixing in our models is modeled following Kippenhahn et al. (1980). Incorporating the default MESA settings for massive star evolution, the corresponding efficiency parameter for thermohaline mixing ( $\alpha_{\text{th}}$ ) is set to 2.0 and 0 for the phases before and after the core-He exhaustion, respectively. The convective overshooting in our models is modeled using the scheme mentioned by Herwig (2000). The overshoot mixing parameters are fixed at  $f_{\text{ov}} = 0.005$  and  $f_0 = 0.001$ . The choice of these values of  $f_{\text{ov}}$  and  $f_0$  closely follows the settings of Farmer et al. (2016) and Aryan et al. (2023). To incorporate the effects of wind, the ‘‘Dutch’’ wind scheme is employed with a wind scaling factor ( $\eta_{\text{wind}}$ ) of 0.5. The choices of these parameters are also primarily followed from prior studies, such as those given in Aguilera-Dena et al. (2018), Perna et al. (2018), and Song & Liu (2023). We have summarized a few of the initial parameters in Table A8.

With the above-mentioned MESA settings and initial parameters, we evolve all the models from PMS up to the stage of the onset of core collapse. The arrival of a model on ZAMS is marked at a stage where the ratio of the luminosity from nuclear reactions and the overall luminosity of the model becomes 0.4. Further, the beginning of the core collapse of the model is marked when the infall velocity of its Fe-core exceeds a limit of  $1000 \text{ km s}^{-1}$ . The left panel of Figure 14 illustrates the evolutionary trajectory of the models in the current study on the H-R diagram. Owing to the low initial metallicity, rotation, and a moderate wind scaling factor ( $\eta_{\text{wind}} = 0.5$ ), most of the models terminate their evolution toward the relatively hotter end on the H-R diagram, except the 15, 20, and 25  $M_{\odot}$  models

having an angular rotational velocity  $\leq 0.2 \Omega_c$ . These slowly rotating models with ZAMS mass ( $M_{\text{ZAMS}}$ ) of 15, 20, and 25  $M_{\odot}$  end their evolutions toward the cooler side of the H-R diagram. These models also possess large final radii ( $R_{\text{final}}$ ) at their terminating stages, as indicated in the right panel of Figure 14. As listed in Table A8, the final radii of these slowly rotating models exceed several  $100 R_{\odot}$ ; thus indicating they terminate their evolution as massive RSGs. All the models in our simulations exceed the final radii of  $10^{11} \text{ cm}$ , which is a consistent result for ULGRB progenitors (Gottlieb et al. 2022). However, models terminating their evolution as RSGs cease to serve as the progenitors for the GRBs/ULGRBs since their enormous final radii ( $t_b > 100 \text{ s}$ , Table A8) do not allow successful penetration of the jet. Thus, the slowly rotating models with  $M_{\text{ZAMS}}$  of 15, 20, and 25  $M_{\odot}$  are discarded as the progenitors of ULGRBs.

Utilizing the simulation parameters of the models at the stage of the onset of core collapse, we estimate the freefall timescales ( $t_{\text{ff}}$ ) by employing Equation (1) of Perna et al. (2018). The  $t_{\text{ff}}$  for each model is listed in Table A8. The estimation of  $t_{\text{ff}}$  is important to gain insights into how long the central engine can be fueled; thus, it can be compared with the  $T_{90}$  duration of the GRBs. In a recent work by Song & Zhang (2023), the authors propose a two-stage model for GRB 221009A and associate the precursor pulse with the weak jet arising due to the collapsed core. Thus, we estimate the bore-time ( $t_b$ ) of the weak jet for each of our models to get insight into the precursor pulse. We estimate  $t_b$  using a simple equation:

$$t_b = \frac{R_{\text{final}}}{(u\Gamma)}. \quad (3)$$

In the above equation,  $u$  is the weak jet velocity corresponding to a Lorentz factor of  $\Gamma$ . The factor  $\Gamma$  is divided in the denominator to account for the relativistic length contraction. While calculating the  $t_b$  using Equation (3) above, we make a very simplified assumption that the weak jet moves with a

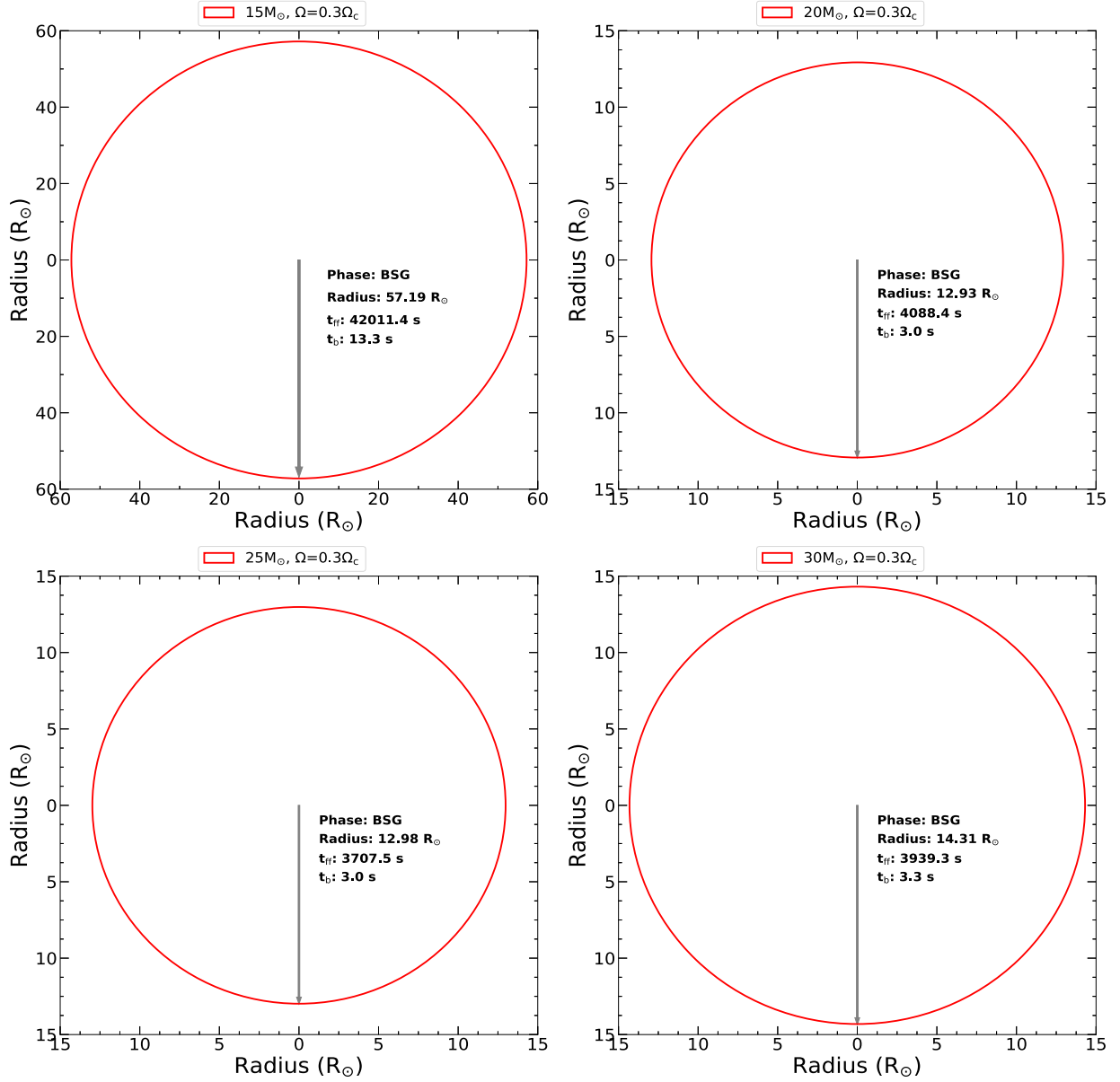


**Figure 15.** The radii of four models from the set of entire models, having  $M_{\text{ZAMS}}$  of 15, 20, 25, and 30  $M_{\odot}$  respectively at the stage of the onset of core collapse. The  $t_{\text{ff}}$  and  $t_b$  for each model are also indicated. We have assumed a  $\Gamma = 10$  for each model while estimating  $t_b$ .

constant  $\Gamma$  of 10. The choice of  $\Gamma = 10$  is motivated from Song & Zhang (2023), where the authors mention that, at the time of break out, the  $\Gamma$  is of the order of 10. With these assumptions, the estimated  $t_b$  for each model is listed in Table A8. Within the range of employed MESA settings and initial parameters, in Figure 15, we have depicted the final stages of four models from the set of entire models, having  $M_{\text{ZAMS}}$  of 15, 20, 25, and 30  $M_{\odot}$ , and each one of them having  $\Omega = 0.3 \Omega_c$ . The final radius,  $t_{\text{ff}}$ , and  $t_b$  are also indicated in the figure.

The above calculations are made for jet bore-time ( $t_b$ ) considering that the Lorentz factor within the envelope remains almost constant to its initial value ( $\Gamma_0 = 10$ ), independent of the mass and radius of the stars. However, in reality, the Lorentz factor of a fireball depends on the distance from the center of the star. Initially, during the expansion of the shell, i.e., coasting phase, the Lorentz factor of the fireball remains almost constant to the initial value  $\Gamma_0$  (Lin et al. 2019). After some

time, known as deceleration time  $t_{\text{dec}}$ , the fireball enters in the self-similar expansion (Blandford & McKee 1976), and the Lorentz factor of the jet evolves with the radius of star by the relation  $\Gamma \propto R^{-3/2}$  (for  $T_{90} < t_{\text{dec}}$ ) or  $R^{-1/2}$  (for  $T_{90} > t_{\text{dec}}$ ) (Mészáros 2006). This indicates that, as the radius increases, the Lorentz factor of the fireball decreases, that eventually increases the corresponding  $t_b$ . Thus, the quoted values of  $t_b$  in our work are obviously the lower limits of bore-time for the underlying Jets.

Now, we compare the  $t_{\text{ff}}$  estimated from our simulation parameters with a few actual  $T_{90}$  duration of our gold sample of ULGRBs mentioned in Table A1. The model with  $M_{\text{ZAMS}} = 30 M_{\odot}$  and  $\Omega = 0.4 \Omega_c$  has a  $t_{\text{ff}}$  of  $\sim 4540$  s, which is close to the  $T_{90}$  duration of GRB 070419B; the model with  $M_{\text{ZAMS}} = 30 M_{\odot}$  and  $\Omega = 0.2 \Omega_c$  has a  $t_{\text{ff}}$  of  $\sim 42,500$  s, which is close to the  $T_{90}$  duration of GRB 090404. Moreover, the  $t_{\text{ff}}$  obtained from our considered models are of similar order when

compared to the actual  $T_{90}$  durations of our gold sample of ULGRBs.

## 6. Summary and Conclusion

The underlying physical mechanism, possible progenitor, and central engine of ULGRBs are still unclear. Previous findings have shown that ULGRBs, despite their exceptionally longer prompt emission duration, exhibit prompt and afterglow spectra, surrounding environment, and host properties similar to LGRBs. This paper aims to constrain the possible progenitor and central engine of GRB 221009A and other similar bursts exhibiting ULGRB characteristics based on their observed  $T_{90}$  durations. In this context, we present a comprehensive search for ULGRB candidates using Swift-detected GRBs (the most updated and complete sample). Specifically, we focus on GRBs with  $T_{90}$  durations exceeding the mean value derived from a Gaussian distribution of Swift-detected LGRBs with redshift measurements. Our sample incorporates a total of  $\sim 230$  GRBs. The selected GRBs are subsequently categorized into bronze, silver, and gold subsamples based on their  $T_{90}$  duration, which lies in the  $1\sigma$ ,  $2\sigma$ , and  $3\sigma$  confidence levels of the distribution. For sample completeness, we included known cases of ULGRBs as the diamond sample. After sample selection, we performed the detailed prompt and afterglow analyses of GRB 221009A and the GRBs listed in our different subsamples utilizing space-based data from Swift and Fermi satellites.

The prompt temporal and spectral examination of GRB 221009A revealed an ultralong nature with a precursor activity, and for this precursor emission, the Band function best describes the spectra while incorporating the thermal component into the Band function only slightly improves the spectral fitting. Nevertheless, the evolution of  $\alpha_{\text{pt}}$  and  $E_{\text{pt}}$  during the precursor and main pulse of GRB 221009A suggests a potential synchrotron origin for the prompt emission (Song & Zhang 2023). It is noteworthy that both  $\alpha_{\text{pt}}$  and  $E_{\text{pt}}$  exhibit flux-tracking evolution.

The distribution of spectral parameters obtained from the prompt and afterglow emission analysis of the bronze, silver, and gold subsamples is consistent with the broad sample of GRBs in the background (see Figures 6 and A3). In the HR- $T_{90}$  space as plotted in Figure 5, SGRBs are harder than LGRBs (a well-known feature of two classical families of GRBs), and the bronze and silver subsamples are consistent with LGRBs, implying they might represent similar kinds of bursts as expected. However, GRBs in our gold subsample show an overall soft spectral characteristic (including GRB 221009A). Again, in the fluence- $T_{90}$  space, GRBs included in SGRBs, LGRBs, bronze, and silver subsamples are showing an increasing trend while the GRBs in gold subsamples are deviating from this trend. This might hint that the gold subsample consists of GRBs with soft spectral characteristics, and they are relatively fainter than the other bursts, making them potential candidates for a new class of so-called ULGRBs. Furthermore, to constrain the origin of GRB 221009A and the GRBs in our bronze, silver, and gold subsamples, we have utilized the following methods:

First, we conducted a comparative analysis of the NIR light curve of GRB 221009A (including our observations taken using 3.6 m Devasthal Optical Telescope, hereafter DOT) with that of other GRBs associated with SNe. The NIR light curve of GRB 221009A exhibited a smooth decay, distinguishing it from other SN-detected GRBs where distinct bumps and

flattening were observed. Our late-time NIR observations obtained with 3.6 m DOT and publicly available data rule out the presence of any prominent SN associated with GRB 221009A. Subsequently, utilizing prompt and afterglow analyses, we attempted to constrain the progenitor of GRBs (collapsar or merger) within our subsamples. GRB emission is accompanied by an ultrarelativistic jet that must bore through the preexisting envelope surrounding the progenitor star. For a GRB to have a collapsar origin, the central engine powering the burst must remain active for a period longer than the jet boretime. In other words,  $T_{90}$  must be greater than  $t_b$ . We first constrained the jet opening angle by utilizing the jet break time observed in the X-ray afterglow light curve, the isotropic energy release during the prompt emission, and other observed properties. Then, using Equation (1), we calculated the  $t_b$ . The obtained values of  $t_b$  found much less than  $T_{90}$  lead to the collapsar origin of all the bursts, including GRB 221009A. To further strengthen these results, we calculated the probabilities of noncollapsar origin for all GRBs included in our sample. The negligible values of noncollapsar probability again confirmed their collapsar origin. To further confirm our analysis results, we simulated the evolution of the low-metallicity massive star having  $M_{\text{ZAMS}}$  of 15, 20, 25, and  $30 M_{\odot}$  and different initial rotations utilizing MESA. The boretime obtained from the simulation closely matches our analysis results in Section 4.2. Subsequently, utilizing the simulation parameters of our models when they entered the core-collapse phase, we estimated the freefall time ( $t_{\text{ff}}$ ). Notably, a significantly extended final radius and  $t_{\text{ff}}$  observed in slowly rotating stars ( $\Omega \leq 0.2, \Omega_c$ ) that evolved to RSG contradict their potential to produce ultrarelativistic jets and their penetration through the surrounding envelope. For moderately rotating stars ( $\Omega \geq 0.2, \Omega_c$ ), the  $t_{\text{ff}}$  obtained from our simulated models closely matches the actual  $T_{90}$  of a few ULGRBs from our gold sample. These findings suggest that rotating ( $\Omega \geq 0.2 \Omega_c$ ) massive stars could potentially be the progenitors of ULGRBs within the considered parameters and initial inputs to MESA.

To constrain the central engine associated with the GRBs in our gold, silver, and bronze subsamples, we have utilized the following methods: (1) For Fermi-GBM detected bursts (32 GRBs), we calculated the isotropic gamma-ray energy  $E_{\gamma, \text{iso}}$  and beaming corrected energy  $E_{\theta_p, \gamma, \text{iso}} \sim \theta_j^2/2 \times E_{\gamma, \text{iso}}$ . For GRBs with  $E_{\theta_p, \gamma, \text{iso}} < 2 \times 10^{52}$  erg, a magnetar can be the possible central engine for these bursts. For  $E_{\theta_p, \gamma, \text{iso}} > 2 \times 10^{52}$  erg, a magnetar central engine is not possible due to its maximum energy constrain, and a black hole central engine is favored. In this case, only two GRBs, GRB 210619B and GRB 221009A, cannot be explained by a magnetar and require a black hole engine with black hole masses  $\sim 3.4 M_{\odot}$  and  $\sim 9.1 M_{\odot}$ , respectively. (2) For 74 GRBs (47 bronze, 21 silver, six gold) with the plateau in the Swift-XRT light curve, we calculated the isotropic X-ray energy  $E_{\text{X, iso}}$  released during the plateau phase as well as the kinetic energy  $E_{\text{K, iso}}$  of the burst. A magnetar central engine is favored by GRBs with  $E_{\text{X, iso}} < 2 \times 10^{52}$  erg and  $E_{\text{K, iso}} < 2 \times 10^{52}$  erg. For GRBs with  $E_{\text{X, iso}} > 2 \times 10^{52}$  erg and  $E_{\text{K, iso}} > 2 \times 10^{52}$  erg, a black hole engine is preferred. A black hole central engine is poorly constrained for the rest of the GRBs. In this case, a hyperaccreting black hole is constrained as a potential central engine candidate for our gold samples, and only a few GRBs (GRB 060218, GRB 100316D, and GRB 091024A) favor a magnetar.

In summary, utilizing  $T_{90}$  as prevailing criteria, we present a method to search for ULGRB candidates. The observed properties of GRB 221009A (the brightest burst ever observed) are also discussed in this context. Further, we shed light on the origin and central engines of ULGRBs and the population of LGRBs. To achieve this, we statistically examine a nearly complete sample of Swift-detected GRBs and categorize them into bronze, silver, and gold subsamples. The properties of GRBs in the bronze subsample do not show any difference from the LGRB population. Our gold subsample indicates a higher likelihood of belonging to the ULGRB category. We successfully constrain the collapsar origin for all GRBs in our sample. Specifically, we found a hyperaccreting black hole central engine for GRB 221009A, featuring a black hole mass of  $\sim 9.1M_{\odot}$ . Similarly, most GRBs in our gold subsample favor a black hole central engine, except for three GRBs (GRB 060218, GRB 100316D, and GRB 091024A). In addition, the distribution of  $N_{\text{H},z}$  and  $A_{\text{v,Host}}$  does not favor any particular kind of low-density environment for the GRBs in the gold subsample, as suggested by Evans et al. (2014). Moreover, the striking similarities obtained in the observed parameters and simulation results from MESA provide additional support for the low-metallicity and rotating ( $\Omega \geq 0.2 \Omega_{\text{c}}$ ) massive stars as progenitors for ULGRBs. It is also cautioned that, except  $T_{90}$  duration, the present analysis did not find any other robust criteria to distinguish between LGRBs and ULGRBs, and there could be other potential observed parameters to demarcate between the two populations of GRBs. Instead, we proposed a method to compare the properties of the GRB subsamples with the increasing likelihood of being ULGRB candidates and understanding the nature of their progenitors. The upcoming Space-based multi-band astronomical Variable Objects Monitor mission is expected to detect more ULGRBs (at higher redshift) and provide insight into unusually long emissions from these bursts (Dagoneau et al. 2020).

### Acknowledgments

R.G. and S.B.P. acknowledge the financial support of ISRO under AstroSat archival Data utilization program (DS \_ 2B-13013(2)/1/2021-Sec.2). S.B.P. also acknowledges support from DST grant No. DST/ICD/BRICS/Call-5/CoNMu-TraMO/2023(G) for the present work. A.K.R. and R.G. are thankful to Dr. Amy Lien for updating the Swift-BAT GRB catalog page on request and fruitful suggestions on the results. R.G. is also grateful to Dr. M. J. Moss for the discussion. R.G. was sponsored by the National Aeronautics and Space Administration (NASA) through a contract with ORAU. The views and conclusions contained in this document are those of the authors and should not be interpreted as representing the official policies, either expressed or implied, of the National Aeronautics and Space Administration (NASA) or the U.S. Government. The U.S. Government is authorized to reproduce and distribute reprints for Government purposes notwithstanding any copyright notation herein. A.A. acknowledges funds and assistance provided by the Council of Scientific & Industrial Research (CSIR), India, under file No. 09/948 (0003)/2020-EMR-I. A.A. also acknowledges the Yushan Young Fellow Program by the Ministry of Education, Taiwan, for financial support. A.J.C.T. acknowledges support from the Spanish Ministry project PID2020-118491GB-I00 and Junta de Andalucía grant P20\_010168. This research has used data obtained through the HEASARC Online Service, provided by

the NASA-GSFC, in support of NASA High Energy Astrophysics Programs. We extend sincere thanks to all the observing and support staff of the 3.6 m DOT to maintain and run the observational facilities at Devasthal Nainital.

The MESA inlists and final models can be found on Zenodo at doi:[10.5281/zenodo.11482190](https://doi.org/10.5281/zenodo.11482190).

*Facilities:* ARIES:DOT, Swift, Fermi.

*Software:* MESA (Paxton et al. 2011, 2013, 2015, 2018; Jermyn et al. 2023), GBM-Tool (Goldstein et al. 2022), 3ML (Vianello et al. 2015), XSPEC (Arnaud 1996), DAOPHOT-II (Stetson 1987), IRAF (Tody 1986, 1993), Matplotlib (Hunter 2007).

## Appendix Multiwavelength Observations and Analysis of GRB 221009A

The Appendix section consists of eight tables and four figures, respectively, Tables A1–A8 and Figures A1–A4. GRB 221009A is the brightest burst observed to date, with  $E_{\gamma,\text{iso}} = 1 \times 10^{55}$  erg and  $L_{\gamma,\text{iso}} = 9.91 \times 10^{53}$  (Lesage et al. 2023). The Swift team initially reported this burst as a detection of a new bright Galactic transient (Dichiara et al. 2022). However, the source was identified as an extremely bright burst based on the strong fading nature of the X-ray counterpart and the simultaneous detection/localization by Fermi-GBM (at 13:16:59.000 UT on 2022 October 9, hereafter  $T_0$ ) and LAT (Kennea & Williams 2022). Due to the delay (about an hour) in the confirmation of the nature of the source post-GBM/BAT trigger, nearly all the ground-based telescopes missed the early emission. However, soon after the Swift and Fermi discovery report of extremely bright GRB 221009A, several space and ground-based telescopes (including 3.6 m DOT facility) started a rigorous follow-up campaign across the electromagnetic band. In this section, we present the detailed analyses of space (Swift and Fermi) and ground-based observations of GRB 221009A.

### A.1. Prompt Emission: Temporal and Spectral Analysis

We acquired the Fermi-GBM data for GRB 221009A from the Fermi-GBM Burst Catalog<sup>15</sup> and conducted a temporal and spectral data analysis using the techniques outlined in Gupta et al. (2022a) and Gupta (2023). To perform the temporal and spectral analysis on the GBM data, we employed the Python-based package GBM-TOOL (Goldstein et al. 2022), focusing on the brightest sodium iodide detectors (NaI-7) as well as the brightest bismuth germanate detector (BGO-1). The multi-channel Fermi-GBM light curves of GRB 221009A are shown in Figures A1 and A2. The Fermi-GBM light curve of GRB 221009A consists of a faint precursor emission followed by a main and extremely bright emission episode. We noted that the counts remain above the background or even consist of very faint and weaker emission in between the precursor and the main burst, started at  $\sim T_0 + 180$  s (see inset in the left panel of Figure A2). This is important and proves that, in the past, this has been missed for other bursts with precursors due to the combination of higher  $z$  and sensitivity limits of detectors. Figure A1 shows the Fermi count-rate light curve in different energy ranges and the evolution of the HR. During the main and very long (more than 1000 s) emission phase of

<sup>15</sup> <https://heasarc.gsfc.nasa.gov/W3Browse/fermi/fermigbrst.html>

**Table A1**  
The Characteristics of the ULGRBs in Our Sample That Met the Selection Criteria Given in Section 2

GRB	$z$	$T_{90}$ (s)	$E_{\gamma,iso}$ ( $\times 10^{52}$ erg)	$L_{\gamma,iso}$ ( $\times 10^{51}$ erg s $^{-1}$ )	$E_{K,iso}$ ( $\times 10^{52}$ erg)	$E_{X,iso}$ ( $\times 10^{50}$ erg)	$\frac{T_{90,z}}{t_b}$	Noncollapsar Probability
Bronze Sample								
050315	1.95	95.4	14.95 $\pm$ 0.66	5.28 $\pm$ 0.64	...	...	30.88	6.21 $\times 10^{-8}$
050319	3.2425	152	15.12 $\pm$ 1.65	10.12 $\pm$ 1.60	...	...	34.53	6.43 $\times 10^{-9}$
050505	4.2748	58.9	44.16 $\pm$ 3.28	29.62 $\pm$ 4.43	...	...	15.37	5.94 $\times 10^{-7}$
050724	0.257	98.7	0.08 $\pm$ 0.01	0.19 $\pm$ 0.02	...	...	12.42	5.27 $\times 10^{-8}$
050730	3.9693	155	37.23 $\pm$ 2.45	7.26 $\pm$ 1.99	...	273.00 $\pm$ 11.00	79.9	5.84 $\times 10^{-9}$
050803	3.5	88.1	27.83 $\pm$ 1.74	10.50 $\pm$ 1.42	...	...	17.64	9.08 $\times 10^{-8}$
050814	5.3	143	47.16 $\pm$ 5.19	11.93 $\pm$ 4.88	...	...	46.48	8.69 $\times 10^{-9}$
Silver Sample								
050820A	2.6147	241	30.31 $\pm$ 1.94	17.97 $\pm$ 2.06	70.00 $\pm$ 20.00	100.98 $\pm$ 11.31	80.67	6.65 $\times 10^{-10}$
050904	6.295	182	166.20 $\pm$ 6.38	17.16 $\pm$ 4.88	...	...	46.45	2.65 $\times 10^{-9}$
051001	2.4296	190	12.27 $\pm$ 1.01	2.47 $\pm$ 0.65	...	...	34.74	2.14 $\times 10^{-9}$
060202	0.783	193	1.78 $\pm$ 0.13	0.34 $\pm$ 0.11	...	...	24.4	1.98 $\times 10^{-9}$
060210	3.9122	288	118.40 $\pm$ 6.32	18.19 $\pm$ 4.03	...	...	75.11	2.80 $\times 10^{-10}$
060510B	4.941	263	88.33 $\pm$ 3.66	10.01 $\pm$ 2.27	...	...	51.6	4.34 $\times 10^{-10}$
060526	3.2213	298	14.51 $\pm$ 1.86	15.52 $\pm$ 1.80	...	...	177.27	2.37 $\times 10^{-10}$
Gold Sample								
060124A	2.29	750	4.36 $\pm$ 0.79	6.73 $\pm$ 2.59	...	...	281.16	4.42 $\times 10^{-12}$
060218A	0.034	2100	0.003 $\pm$ 0.0003	0.47 $\pm$ 0.96	0.47 $\pm$ 0.096	2.57 $\pm$ 0.01	210.6	1.09 $\times 10^{-12}$
070419B	1.9588	4930	57.61 $\pm$ 2.38	11.38 $\pm$ 2.69	56.00 $\pm$ 14.00	17.19 $\pm$ 0.85	3018.07	4.43 $\times 10^{-10}$
070518A	1.16	57,900	0.40 $\pm$ 0.09	0.98 $\pm$ 0.35	...	...	6413.03	...
080319B	0.938	1340	238.60 $\pm$ 4.05	68.57 $\pm$ 2.43	...	...	2119.36	1.02 $\times 10^{-12}$
090404A	2.87	44,700	35.90 $\pm$ 1.90	18.27 $\pm$ 2.78	...	...	21,417.06	...
090417B	0.345	2130	0.48 $\pm$ 0.06	0.04 $\pm$ 0.03	...	...	117.79	1.12 $\times 10^{-12}$
091024A	1.09	1300	20.00 $\pm$ 1.64	6.60 $\pm$ 1.64	21.00	...	714.02	1.06 $\times 10^{-12}$
091127A	0.49	5398	3.53 $\pm$ 0.20	13.47 $\pm$ 1.16	...	...	4372.42	1.74 $\times 10^{-9}$
100316D	0.059	1300	0.004 $\pm$ 0.001	0.003 $\pm$ 0.0004	0.004	0.002	36.43	1.06 $\times 10^{-12}$
100728A	1.57	1460	267.78 $\pm$ 5.53	51.85 $\pm$ 4.58	...	...	1039.18	9.34 $\times 10^{-13}$
101225A	0.85	6420	2.94 $\pm$ 0.98	...	64.5	...	...	...
111209A	0.677	18,200	38.79 $\pm$ 0.95	0.72 $\pm$ 0.44	96.00	50.80 $\pm$ 0.60	2707.35	...
111215A	2.1	1120	24.36 $\pm$ 5.36	4.08 $\pm$ 3.34	...	...	214.15	1.39 $\times 10^{-12}$
121027A	1.773	5730	12.96 $\pm$ 1.26	5.81 $\pm$ 1.48	90.64 $\pm$ 22.97	207.00 $\pm$ 8.00	2104.28	4.77 $\times 10^{-9}$
121217A	3.1	778	112.93 $\pm$ 9.45	25.44 $\pm$ 4.06	...	...	627.18	3.90 $\times 10^{-12}$
130925A	0.348	4500	6.01 $\pm$ 0.19	0.99 $\pm$ 0.14	0.50	...	1206.36	1.35 $\times 10^{-10}$
140614A	4.233	720	19.42 $\pm$ 3.80	10.33 $\pm$ 14.65	13.78 $\pm$ 4.75	10.00 $\pm$ 1.30	408.2	5.11 $\times 10^{-12}$
141121A	1.47	1410	12.06 $\pm$ 2.67	2.36 $\pm$ 1.35	100.00	13.80 $\pm$ 0.86	343.57	1.03 $\times 10^{-12}$
170714A	0.793	1000	3.78 $\pm$ 0.67	0.24 $\pm$ 0.48	...	...	114.28	1.82 $\times 10^{-12}$
210905A	6.32	778	241.61 $\pm$ 51.34	140.22 $\pm$ 45.56	...	...	619.7	3.90 $\times 10^{-12}$
221009A	0.151	1100	1000 $\pm$ 7.00	991 $\pm$ 6.00	541.00 $\pm$ 157.97	...	4270.76	1.45 $\times 10^{-12}$

(This table is available in its entirety in machine-readable form in the [online article](#).)

**Table A2**

Characteristics of a Sample of Well-studied GRBs Included in Our Diamond Subsample Obtained from the Various Published Papers with Corresponding References in the Last Column

GRB	$z$	$T_{90}^*$ (s)	$E_{\gamma,iso}$ (erg)	$E_{K,iso}$ (erg)	$E_{X,iso}$ (erg)	$E_{pt}$ (KeV)	References
090309A	...	5276	...	...	...	...	Lien et al. (2016)
101024A	...	4883	...	...	...	...	Lien et al. (2016)
110709B	...	900	...	...	...	...	Virgili et al. (2013)
220627A	3.08	1092	4.81 $\pm$ 0.02 $\times 10^{54}$	9.01 $\pm$ 7.41 $\times 10^{53}$	2.00 $\times 10^{52}$	205 $\pm$ 109	de Wet et al. (2023)

**Note.**

<sup>a</sup> Durations given in references.

GRB 221009A, most of the GRB detecting instruments, including Fermi-GBM, were saturated, making the prompt emission analysis challenging. Following the analysis by

Lesage et al. (2023), Liu et al. (2023), and Zhang et al. (2023), we omit the interval [217–280 s] and [508–514 s] to avoid pile up. To perform the spectral analysis of Fermi-GBM

**Table A3**  
Parameters Obtained from the Spectral Fitting of Prompt Emission of GRB 221009A with Band and Band + Blackbody Function

$T_{\text{start}}$ (s)	$T_{\text{end}}$ (s)	$\alpha_{\text{pt}}$	$E_{\text{pt}}$ (keV)	$\beta_{\text{pt}}$	$kT$ (KeV)	Photon Flux (photon s <sup>-1</sup> cm <sup>-2</sup> )	Energy Flux (erg s <sup>-1</sup> cm <sup>-2</sup> )	BIC
0	10	-1.724 <sup>+0.023</sup> <sub>-0.023</sub>	1241.579 <sup>+1213.568</sup> <sub>-488.208</sub>	-7.422 <sup>+5.380</sup> <sub>-0.000</sub>	...	11.502	1.90 × 10 <sup>-6</sup>	641.84
10	20	-1.706 <sup>+0.064</sup> <sub>-0.059</sub>	158.330 <sup>+129.004</sup> <sub>-57.429</sub>	-6.115 <sup>+0.000</sup> <sub>-0.000</sub>	...	3.244	2.76 × 10 <sup>-7</sup>	325.05
20	40	-1.711 <sup>+0.050</sup> <sub>-0.046</sub>	93.057 <sup>+40.965</sup> <sub>-26.391</sub>	-10.000 <sup>+0.000</sup> <sub>-0.000</sub>	...	2.656	1.88 × 10 <sup>-7</sup>	422.71
40	120	-1.697 <sup>+0.040</sup> <sub>-0.037</sub>	41.305 <sup>+11.102</sup> <sub>-8.489</sub>	-6.100 <sup>+3.743</sup> <sub>-0.000</sub>	...	1.218	6.51 × 10 <sup>-8</sup>	623.04
120	175	-1.621 <sup>+0.031</sup> <sub>-0.030</sub>	52.615 <sup>+9.056</sup> <sub>-7.467</sub>	-7.359 <sup>+4.865</sup> <sub>-0.000</sub>	...	2.062	1.17 × 10 <sup>-7</sup>	688.46
175	210	-1.119 <sup>+0.005</sup> <sub>-0.005</sub>	565.048 <sup>+5.546</sup> <sub>-5.555</sub>	-2.337 <sup>+0.030</sup> <sub>-0.033</sub>	...	86.41	2.58 × 10 <sup>-5</sup>	17,020.85
210	215	-1.133 <sup>+0.009</sup> <sub>-0.009</sub>	259.168 <sup>+4.513</sup> <sub>-4.439</sub>	-2.255 <sup>+0.044</sup> <sub>-0.044</sub>	...	109.696	2.20 × 10 <sup>-5</sup>	4624.26
280	300	-1.465 <sup>+0.002</sup> <sub>-0.002</sub>	538.138 <sup>+8.768</sup> <sub>-3.667</sub>	-2.209 <sup>+0.015</sup> <sub>-0.015</sub>	...	384.494	7.88 × 10 <sup>-5</sup>	79,848.27
300	330	-1.504 <sup>+0.003</sup> <sub>-0.002</sub>	47.966 <sup>+0.412</sup> <sub>-0.699</sub>	-2.024 <sup>+0.006</sup> <sub>-0.006</sub>	...	111.441	1.33 × 10 <sup>-5</sup>	34,106.81
330	380	-1.281 <sup>+0.002</sup> <sub>-0.002</sub>	41.923 <sup>+0.243</sup> <sub>-0.252</sub>	-2.224 <sup>+0.008</sup> <sub>-0.008</sub>	...	88.713	7.86 × 10 <sup>-6</sup>	50,251.11
380	450	-1.520 <sup>+0.002</sup> <sub>-0.002</sub>	169.723 <sup>+1.591</sup> <sub>-1.525</sub>	-2.220 <sup>+0.015</sup> <sub>-0.014</sub>	...	115.398	1.50 × 10 <sup>-5</sup>	92,334.54
450	465	-1.410 <sup>+0.003</sup> <sub>-0.003</sub>	188.551 <sup>+2.228</sup> <sub>-2.294</sub>	-2.229 <sup>+0.020</sup> <sub>-0.020</sub>	...	194.609	2.80 × 10 <sup>-5</sup>	35,179.5
465	480	-1.530 <sup>+0.003</sup> <sub>-0.003</sub>	317.729 <sup>+6.432</sup> <sub>-3.869</sub>	-3.386 <sup>+1.109</sup> <sub>-0.040</sub>	...	212.591	2.63 × 10 <sup>-5</sup>	42,367.11
480	500	-1.396 <sup>+0.003</sup> <sub>-0.003</sub>	165.436 <sup>+1.529</sup> <sub>-1.741</sub>	-2.247 <sup>+0.017</sup> <sub>-0.018</sub>	...	187.32	2.55 × 10 <sup>-5</sup>	48,050.02
520	555	-1.414 <sup>+0.002</sup> <sub>-0.002</sub>	321.032 <sup>+2.879</sup> <sub>-2.945</sub>	-2.150 <sup>+0.013</sup> <sub>-0.013</sub>	...	217.701	4.05 × 10 <sup>-5</sup>	99,834.32
555	600	-1.479 <sup>+0.002</sup> <sub>-0.002</sub>	125.181 <sup>+0.854</sup> <sub>-1.109</sub>	-2.279 <sup>+0.015</sup> <sub>-0.012</sub>	...	154.187	1.76 × 10 <sup>-5</sup>	111,863.65
170	600	-1.287 <sup>+0.000</sup> <sub>-0.000</sub>	2367.750 <sup>+7.242</sup> <sub>-6.056</sub>	-2.423 <sup>+0.007</sup> <sub>-0.006</sub>	...	314.243	1.52 × 10 <sup>-4</sup>	1,397,389.35

$T_{\text{start}}$ (s)	$T_{\text{end}}$ (s)	$\alpha_{\text{pt}}$	$E_{\text{pt}}$ (keV)	$\beta_{\text{pt}}$	$kT$ (KeV)	Photon Flux (photon s <sup>-1</sup> cm <sup>-2</sup> )	Energy Flux (erg s <sup>-1</sup> cm <sup>-2</sup> )	BIC
0	10	-1.724 <sup>+0.027</sup> <sub>-0.027</sub>	1240.536 <sup>+1579.592</sup> <sub>-540.508</sub>	-7.957 <sup>+0.000</sup> <sub>-0.000</sub>	11.309 <sup>+11.309</sup> <sub>-0.000</sub>	11.502	1.90 × 10 <sup>-6</sup>	653.65
10	20	-1.839 <sup>+0.085</sup> <sub>-0.000</sub>	316.852 <sup>+1940.886</sup> <sub>-231.345</sub>	-5.199 <sup>+0.000</sup> <sub>-0.000</sub>	29.476 <sup>+29.476</sup> <sub>-0.000</sub>	3.28	3.39 × 10 <sup>-7</sup>	337.78
20	40	-1.900 <sup>+0.056</sup> <sub>-0.000</sub>	68.317 <sup>+269.097</sup> <sub>-36.847</sub>	-9.614 <sup>+0.000</sup> <sub>-0.000</sub>	22.339 <sup>+22.339</sup> <sub>-0.000</sub>	2.66	1.95 × 10 <sup>-7</sup>	433.12
40	120	-1.699 <sup>+0.047</sup> <sub>-0.043</sub>	41.067 <sup>+13.423</sup> <sub>-9.605</sub>	-10.000 <sup>+7.725</sup> <sub>-0.000</sub>	7.090 <sup>+7.090</sup> <sub>-0.000</sub>	1.218	6.49 × 10 <sup>-8</sup>	634.84
120	175	-0.516 <sup>+0.000</sup> <sub>-0.000</sub>	499.964 <sup>+0.000</sup> <sub>-0.000</sub>	-2.500 <sup>+0.000</sup> <sub>-0.000</sub>	29.418 <sup>+29.418</sup> <sub>-2.820</sub>	0.693	9.00 × 10 <sup>-8</sup>	1359.53
175	210	-1.230 <sup>+0.005</sup> <sub>-0.005</sub>	950.288 <sup>+17.382</sup> <sub>-17.305</sub>	-2.679 <sup>+0.085</sup> <sub>-0.097</sub>	38.465 <sup>+38.465</sup> <sub>-0.444</sub>	86.881	2.63 × 10 <sup>-5</sup>	16,741.2
210	215	-1.134 <sup>+0.010</sup> <sub>-0.010</sub>	259.616 <sup>+5.397</sup> <sub>-5.128</sub>	-2.251 <sup>+0.048</sup> <sub>-0.056</sub>	17.538 <sup>+17.538</sup> <sub>-0.000</sub>	109.654	2.21 × 10 <sup>-5</sup>	4636.08
280	300	-1.471 <sup>+0.002</sup> <sub>-0.003</sub>	563.222 <sup>+7.250</sup> <sub>-6.983</sub>	-2.228 <sup>+0.019</sup> <sub>-0.019</sub>	25.975 <sup>+25.975</sup> <sub>-0.000</sub>	384.667	7.88 × 10 <sup>-5</sup>	79,852.25
300	330	-1.570 <sup>+0.004</sup> <sub>-0.004</sub>	125.862 <sup>+2.032</sup> <sub>-3.415</sub>	-2.079 <sup>+0.017</sup> <sub>-0.018</sub>	5.672 <sup>+5.672</sup> <sub>-0.040</sub>	110.641	1.27 × 10 <sup>-5</sup>	33,905.29
330	380	-1.151 <sup>+0.003</sup> <sub>-0.003</sub>	67.959 <sup>+0.448</sup> <sub>-0.546</sub>	-2.318 <sup>+0.015</sup> <sub>-0.016</sub>	4.510 <sup>+4.510</sup> <sub>-0.022</sub>	88.57	7.43 × 10 <sup>-6</sup>	49,888.79
380	450	-1.520 <sup>+0.002</sup> <sub>-0.002</sub>	170.098 <sup>+1.832</sup> <sub>-1.823</sub>	-2.222 <sup>+0.018</sup> <sub>-0.017</sub>	25.866 <sup>+25.866</sup> <sub>-0.000</sub>	115.403	1.49 × 10 <sup>-5</sup>	92,346.29
450	465	-1.420 <sup>+0.004</sup> <sub>-0.004</sub>	195.499 <sup>+2.237</sup> <sub>-3.520</sub>	-2.244 <sup>+0.023</sup> <sub>-0.028</sub>	25.368 <sup>+25.368</sup> <sub>-0.000</sub>	194.662	2.79 × 10 <sup>-5</sup>	35,194.32
465	480	-1.207 <sup>+0.005</sup> <sub>-0.005</sub>	214.797 <sup>+2.319</sup> <sub>-2.206</sub>	-2.239 <sup>+0.022</sup> <sub>-0.023</sub>	6.342 <sup>+6.342</sup> <sub>-0.040</sub>	209.6	3.11 × 10 <sup>-5</sup>	41,367.58
480	500	-1.090 <sup>+0.005</sup> <sub>-0.005</sub>	166.160 <sup>+1.363</sup> <sub>-1.315</sub>	-2.262 <sup>+0.019</sup> <sub>-0.018</sub>	5.969 <sup>+5.969</sup> <sub>-0.033</sub>	185.27	2.53 × 10 <sup>-5</sup>	47,310.49
520	555	1.287 <sup>+0.004</sup> <sub>-0.004</sub>	110.254 <sup>+0.151</sup> <sub>-0.158</sub>	-2.000 <sup>+0.000</sup> <sub>-0.000</sub>	5.941 <sup>+5.941</sup> <sub>-0.009</sub>	214.325	4.29 × 10 <sup>-5</sup>	101,515.36
555	600	-1.135 <sup>+0.003</sup> <sub>-0.003</sub>	133.009 <sup>+0.811</sup> <sub>-0.805</sub>	-2.303 <sup>+0.015</sup> <sub>-0.014</sub>	5.301 <sup>+5.301</sup> <sub>-0.019</sub>	152.857	1.74 × 10 <sup>-5</sup>	110,518.52
170	600	-1.216 <sup>+0.001</sup> <sub>-0.001</sub>	1975.222 <sup>+6.313</sup> <sub>-4.828</sub>	-2.342 <sup>+0.005</sup> <sub>-0.006</sub>	6.910 <sup>+6.910</sup> <sub>-0.015</sub>	313.455	1.49 × 10 <sup>-4</sup>	1,387,598.57

observations, we have utilized several empirical and physical models to fit the time-integrated and time-resolved spectrum (to observe the spectral parameter evolution) of GRB 221009A. Since this burst lasts longer than 1000 s, we have used CSPECfiles to represent the count-rate light curve and spectral analysis. The fit statistic PGstat is used, and Bayesian Information Criteria (BIC) was applied to find the best-fit model. The time average spectrum (8 keV–40 MeV) in the temporal range  $T_0 + 170$  s– $T_0 + 600$  s is best fit by the Band function, showing the lowest BIC value of all the fits.

The evolution of spectral parameters serves as a crucial tool for deciphering emission mechanisms during the prompt phase of GRBs (Pe'er 2015). The analysis results of Golenetskii et al. (1983), Laros et al. (1985), and Norris et al. (1986) revealed that, within the Band function, the peak energy ( $E_{\text{pt}}$ ) exhibits four distinct types of evolution: (a) transitioning from hard to soft, (b) following flux variations, (c) shifting from soft to hard, and (d) displaying chaotic patterns. Conversely, the evolution of the low-energy spectral index ( $\alpha_{\text{pt}}$ ) is less predictable;

however, some studies have noted flux-tracking patterns in  $\alpha_{\text{pt}}$ , for example GRB 140102A (Gupta et al. 2021a) and GRB 201216C (Ror et al. 2023).

In our analysis of time-resolved spectra, we divided the light curve into multiple time intervals of varying durations (see Table A3). Each interval's spectrum was fitted using different empirical functions, such as the Band function and Cutoff power-law, and subsequently reevaluated by incorporating the thermal Blackbody component. The spectral parameters obtained from the fitting are listed in Table A3. Figures A2 and A3 illustrate the spectral parameter obtained from the best-fit model, showing that both  $E_{\text{pt}}$  and  $\alpha_{\text{pt}}$  seem to track the intensity for GRB 221009A. We observed that the spectrum created near the peak of the light curve is best described by a combination of the Band function and Blackbody, whereas, between the peaks, a single Band function provides the best fit for the spectra. This pattern has been observed in other extensively studied VHE-detected GRBs such as 180720B (Chen et al. 2021) and GRB 201216C (Ror et al. 2023). Our prompt

**Table A4**

Parameters Obtained from the Spectral Fitting of Nonsaturated Precursor Emission of GRB 221009A with Band, Band + Blackbody, Physical synchrotron Model

Band							
$T_{\text{start}}$ (s)	$T_{\text{end}}$ (s)	$\alpha_{\text{pt}}$	$E_{\text{pt}}$ (keV)	$\beta_{\text{pt}}$	...	Flux (erg s <sup>-1</sup> cm <sup>-2</sup> )	BIC
0	10	-1.661 <sup>+0.016</sup> <sub>-0.016</sub>	1531.055 <sup>+292.657</sup> <sub>-284.783</sub>	-3.093 <sup>+0.502</sup> <sub>-0.501</sub>	...	2.48 <sup>+0.12</sup> <sub>-0.13</sub> × 10 <sup>-6</sup>	2697
10	20	-1.701 <sup>+0.069</sup> <sub>-0.071</sub>	838.774 <sup>+473.362</sup> <sub>-476.816</sub>	-3.001 <sup>+0.566</sup> <sub>-0.558</sub>	...	3.07 <sup>+0.51</sup> <sub>-0.58</sub> × 10 <sup>-7</sup>	2617
Band + Blackbody							
$T_{\text{start}}$ (s)	$T_{\text{end}}$ (s)	$\alpha_{\text{pt}}$	$E_{\text{pt}}$ (keV)	$\beta_{\text{pt}}$	$kT$ (KeV)	Flux (erg s <sup>-1</sup> cm <sup>-2</sup> )	BIC
0	10	-1.555 <sup>+0.039</sup> <sub>-0.037</sub>	1205.956 <sup>+252.291</sup> <sub>-250.925</sub>	-3.009 <sup>+0.388</sup> <sub>-0.414</sub>	3.761 <sup>+0.271</sup> <sub>-0.589</sub>	2.46 <sup>+0.28</sup> <sub>-0.23</sub> × 10 <sup>-6</sup>	2685
10	20	-1.758 <sup>+0.089</sup> <sub>-0.087</sub>	931.427 <sup>+437.622</sup> <sub>-433.363</sub>	-2.878 <sup>+0.539</sup> <sub>-0.573</sub>	15.072 <sup>+8.323</sup> <sub>-8.888</sub>	2.98 <sup>+0.49</sup> <sub>-0.42</sub> × 10 <sup>-7</sup>	2595
Cutoff powerlaw							
$T_{\text{start}}$ (s)	$T_{\text{end}}$ (s)	$\alpha_{\text{pt}}$	$E_{\text{pt}}$ (KeV)	...	...	Flux (erg s <sup>-1</sup> cm <sup>-2</sup> )	BIC
0	10	-1.598 <sup>0.0168</sup> <sub>-0.017</sub>	1309.932 <sup>130.161</sup> <sub>-130.35</sub>	...	...	1.80 <sup>0.22</sup> <sub>-0.22</sub> × 10 <sup>-6</sup>	2746
10	20	-1.641 <sup>0.098</sup> <sub>-0.098</sub>	572.897 <sup>170.357</sup> <sub>-171.438</sub>	...	...	1.91 <sup>0.89</sup> <sub>-2.48</sub> × 10 <sup>-7</sup>	2621
Cutoff powerlaw + Blackbody							
$T_{\text{start}}$ (s)	$T_{\text{end}}$ (s)	$\alpha_{\text{pt}}$	$E_{\text{pt}}$ (KeV)	...	$kT$ (KeV)	Flux (erg s <sup>-1</sup> cm <sup>-2</sup> )	BIC
0	10	-1.596 <sup>0.016</sup> <sub>-0.016</sub>	1299.694 <sup>125.674</sup> <sub>-125.262</sub>	...	10.804 <sup>7.889</sup> <sub>-7.276</sub>	1.80 <sup>0.25</sup> <sub>-0.21</sub> × 10 <sup>-6</sup>	2722
10	20	-1.627 <sup>0.097</sup> <sub>-0.098</sub>	564.421 <sup>173.628</sup> <sub>-171.011</sub>	...	11.431 <sup>8.051</sup> <sub>-7.734</sub>	1.99 <sup>2.78</sup> <sub>-0.94</sub> × 10 <sup>-7</sup>	2599
Synchrotron							
$T_{\text{start}}$ (s)	$T_{\text{end}}$ (s)	$B$ (G)	$p$	$\gamma_{\text{cool}}$	...	Flux (erg s <sup>-1</sup> cm <sup>-2</sup> )	BIC
0	10	0.343 <sup>+0.169</sup> <sub>-0.161</sub>	1.681 <sup>+0.629</sup> <sub>-0.611</sub>	34, 957, 576.163 <sup>+48.641, 616.967</sup> <sub>-34.813, 370.352</sub>	...	2.66 <sup>+0.13</sup> <sub>-0.12</sub> × 10 <sup>-6</sup>	2718
10	20	0.924 <sup>+0.043</sup> <sub>-0.902</sub>	1.703 <sup>+0.493</sup> <sub>-0.479</sub>	7, 294, 590.381 <sup>+3.587, 786.823</sup> <sub>-7.099, 455.667</sub>	...	2.58 <sup>+0.61</sup> <sub>-0.47</sub> × 10 <sup>-7</sup>	2626

**Table A5**

Our NIR Observations of GRB 221009A Using 3.6 m DOT at ARIES

$T-T_0$ (days)	Exposure (s)	Filter	Magnitude	Magnitude Error	Telescope
7.05882	200 × 10	<i>R</i>	21.3	0.04	DFOT
13.5428	40 × 50	<i>J</i>	19.70	0.05	DOT
14.5271	40 × 50	<i>J</i>	20.17	0.05	DOT
14.5700	40 × 50	<i>H</i>	19.66	0.09	DOT
16.5497	40 × 50	<i>H</i>	19.65	0.05	DOT
13.6084	20 × 100	<i>K</i>	18.92	0.05	DOT
14.6148	20 × 100	<i>K</i>	18.81	0.08	DOT
15.6124	20 × 100	<i>K</i>	18.96	0.08	DOT
16.6022	20 × 100	<i>K</i>	19.05	0.09	DOT

**Note.** Magnitude is not corrected for Galactic extinction.

emission analysis of GRB 221009A is consistent with the results of Liu et al. (2023) and Zhang et al. (2023).

In the precursor phase of GRB 221009A, we noticed a deviation of the low-energy spectral index from the expected synchrotron fast and slow cooling range ( $-3/2$ ,  $-2/3$ ) (as illustrated in Figure A2), which poses a challenge to explanations involving the synchrotron mechanism (Preece et al. 2002). The spectral fitting outcomes for the precursor

emission are given in Table A4. The Band function provides the best fit for the precursor spectrum. However, adding a Blackbody component to the Band function slightly improves the spectral fitting, indicating the presence of a thermal component in the precursor emission spectrum (Li 2007).

## A.2. Afterglow Analysis of GRB 221009A

In the following section, we provide details of the afterglow follow-up observations of GRB 221009A and the analysis conducted with the 3.6 m DOT (Pandey 2016, 2018) in conjunction with publicly accessible afterglow data.

### A.2.1. DOT NIR Follow-up Observations and Analysis of GRB 221009A

We conducted NIR observations of GRB 221009A using the 3.6 m DOT at ARIES. The burst was observed over five nights, from 2022 October 21 to 26. These observations were made in the *J*, *H*, and *Ks* filters of the TIRCAM2 instrument, which was mounted on the side port of the 3.6 m DOT. We observed source frames at five different dither positions (D1–D5) to remove background noise. Initially, we carried out image preprocessing, for which dark and flat frames were observed separately on every observation night. Subsequently, the dither

**Table A6**  
Prompt Emission Spectral Characteristic of ULGRBs Obtained from the Fitting of Fermi-GBM Observation

Fermi ID	$z$	$T_{90}$ (s)	LAT Boresight (deg)	$\alpha_{pt}$	$E_{pt}$ (keV)	$\beta_{pt}$	$E_{\gamma,iso}$ (erg)
080810549	3.36	107.67	60	$-0.851^{+0.089}_{-0.091}$	$305.672^{+36.751}_{-36.225}$	$-3.101^{+0.507}_{-0.527}$	$62.69^{+14.21}_{-11.17} \times 10^{52}$
080905705	0.12	128	99	$-1.345^{+0.161}_{-0.166}$	$223.605^{+69.603}_{-68.397}$	$-2.856^{+0.639}_{-0.651}$	$0.07^{+0.01}_{-0.01} \times 10^{52}$
080916406	0.69	61.35	76	$-0.981^{+0.074}_{-0.075}$	$120.847^{+9.085}_{-9.144}$	$-3.281^{+0.414}_{-0.432}$	$1.27^{+0.27}_{-0.21} \times 10^{52}$
081008832	1.97	185.5	...	$-0.238^{+0.269}_{-0.264}$	$77.703^{+6.609}_{-6.749}$	$-3.353^{+0.406}_{-0.408}$	$4.33^{+3.66}_{-2.07} \times 10^{52}$
090519881	3.9	64	47	$-0.361^{+0.313}_{-0.314}$	$208.829^{+43.924}_{-44.034}$	$-3.161^{+0.511}_{-0.517}$	$6.61^{+5.2}_{-2.86} \times 10^{52}$
090618353	0.54	113.34	133	$-0.509^{+0.061}_{-0.061}$	$94.387^{+2.922}_{-2.931}$	$-2.123^{+0.015}_{-0.015}$	$25.06^{+3.73}_{-3.18} \times 10^{52}$
090926914	2.11	81	100	$-0.131^{+0.121}_{-0.118}$	$89.572^{+3.921}_{-3.899}$	$-3.512^{+0.331}_{-0.332}$	$2.14^{+0.71}_{-0.52} \times 10^{52}$
091024372	1.09	1020	98	$-0.842^{+0.077}_{-0.076}$	$337.521^{+40.266}_{-40.672}$	$-3.166^{+0.481}_{-0.493}$	$80.97^{+18.13}_{-13.92} \times 10^{52}$
100413732	3.9	184.06	84	$-0.077^{+0.239}_{-0.241}$	$349.718^{+51.801}_{-51.415}$	$-2.917^{+0.571}_{-0.609}$	$76.52^{+38.93}_{-23.85} \times 10^{52}$
100704149	3.6	197.5	64	$-0.489^{+0.144}_{-0.146}$	$175.796^{+16.955}_{-17.286}$	$-3.397^{+0.396}_{-0.401}$	$73.84^{+23.72}_{-17.3} \times 10^{52}$
100814160	1.44	174.5	87	$-0.643^{+0.118}_{-0.118}$	$120.259^{+9.728}_{-9.751}$	$-3.486^{+0.358}_{-0.354}$	$7.77^{+2.32}_{-1.79} \times 10^{52}$
110818860	3.36	103	95	$-1.213^{+0.091}_{-0.091}$	$200.447^{+31.341}_{-30.984}$	$-2.936^{+0.553}_{-0.586}$	$28.27^{+8.53}_{-5.86} \times 10^{52}$
111228657	0.72	101.2	68	$-1.369^{+0.381}_{-0.331}$	$26.903^{+5.182}_{-5.341}$	$-2.633^{+0.328}_{-0.419}$	$1.45^{+3.76}_{-1.02} \times 10^{52}$
120922939	3.11	173	85	$-0.821^{+0.419}_{-0.428}$	$201.682^{+50.354}_{-49.392}$	$-2.719^{+0.481}_{-0.491}$	$34.01^{+4.04}_{-3.85} \times 10^{52}$
130420313	1.29	123.5	134	$-0.808^{+0.361}_{-0.353}$	$56.05^{+10.734}_{-10.652}$	$-3.223^{+0.456}_{-0.474}$	$7.91^{+4.77}_{-2.21} \times 10^{52}$
131105087	1.68	112.3	36	$-1.201^{+0.041}_{-0.041}$	$203.115^{+17.389}_{-17.546}$	$-3.227^{+0.428}_{-0.453}$	$14.16^{+1.92}_{-1.54} \times 10^{52}$
140506880	0.89	111.1	142	$-1.184^{+0.252}_{-0.251}$	$193.196^{+63.929}_{-62.518}$	$-2.969^{+0.584}_{-0.598}$	$1.69^{+1.22}_{-0.65} \times 10^{52}$
140512814	0.72	154.8	...	$-1.261^{+0.037}_{-0.038}$	$392.697^{+48.378}_{-49.035}$	$-3.218^{+0.465}_{-0.483}$	$5.46^{+0.72}_{-0.61} \times 10^{52}$
140703026	3.14	84.04	16	$-1.265^{+0.122}_{-0.121}$	$127.816^{+19.894}_{-19.811}$	$-3.164^{+0.488}_{-0.501}$	$12.18^{+4.24}_{-3.04} \times 10^{52}$
150727793	0.31	49.409	46	$-0.334^{+0.235}_{-0.235}$	$170.106^{+20.908}_{-21.247}$	$-3.111^{+0.492}_{-0.509}$	$0.14^{+0.08}_{-0.05} \times 10^{52}$
151027166	0.81	123.39	9	$-1.375^{+0.102}_{-0.102}$	$172.112^{+37.216}_{-37.495}$	$-2.825^{+0.538}_{-0.604}$	$2.96^{+1.06}_{-0.74} \times 10^{52}$
160804065	0.74	131.58	88	$-1.036^{+0.217}_{-0.217}$	$81.913^{+11.164}_{-11.315}$	$-3.271^{+0.443}_{-0.448}$	$1.58^{+1.12}_{-0.65} \times 10^{52}$
161117066	1.55	122.18	91	$-0.858^{+0.044}_{-0.043}$	$84.824^{+2.297}_{-2.283}$	$-3.597^{+0.282}_{-0.281}$	$14.77^{+1.76}_{-1.56} \times 10^{52}$
170405777	3.51	78.6	52	$-0.662^{+0.037}_{-0.037}$	$257.887^{+14.149}_{-14.122}$	$-2.209^{+0.112}_{-0.109}$	$465.12^{+64.69}_{-60.03} \times 10^{52}$
171222684	2.41	80.452	43	$-1.412^{+0.073}_{-0.073}$	$35.031^{+11.59}_{-11.59}$	$-1.601^{+0.501}_{-0.501}$	$3.41^{+1.82}_{-1.83} \times 10^{52}$
180620660	1.12	46.797	136	$-0.861^{+0.183}_{-0.183}$	$102.944^{+13.173}_{-13.606}$	$-2.671^{+0.356}_{-0.379}$	$2.65^{+1.65}_{-0.96} \times 10^{52}$
180720598	0.65	48.89	50	$-1.023^{+0.011}_{-0.011}$	$633.603^{+17.934}_{-18.142}$	$-2.475^{+0.054}_{-0.054}$	$31.82^{+1.08}_{-1.11} \times 10^{52}$
190114873	0.42	361.5	68	$-1.111^{+0.004}_{-0.004}$	$1069.591^{+19.987}_{-20.043}$	$-3.712^{+0.181}_{-0.187}$	$28.42^{+1.55}_{-1.28} \times 10^{52}$
190829830	0.08	10.37	33	$-0.924^{+0.298}_{-0.285}$	$10.687^{+0.689}_{-0.672}$	$-2.431^{+0.021}_{-0.022}$	$0.02^{+0.02}_{-0.02} \times 10^{52}$
210610827	1.13	55.04	63	$-0.687^{+0.018}_{-0.018}$	$283.452^{+6.948}_{-6.883}$	$-3.441^{+0.355}_{-0.362}$	$17.45^{+1.19}_{-0.88} \times 10^{52}$
210619999	1.94	54.785	108	$-0.913^{+0.013}_{-0.013}$	$226.805^{+6.234}_{-6.033}$	$-2.111^{+0.028}_{-0.028}$	$288.03^{+6.89}_{-7.13} \times 10^{52}$
220101215	4.62	237	18	$-1.028^{+0.043}_{-0.043}$	$305.924^{+27.324}_{-27.224}$	$-3.318^{+0.426}_{-0.438}$	$274.99^{+37.86}_{-29.2} \times 10^{52}$
221009553	0.15	1100	62	$-1.661^{+0.016}_{-0.016}$	$1531.27^{+292.65}_{-284.78}$	$-3.093^{+0.502}_{-0.501}$	$\sim 1000 \times 10^{52}$

(This table is available in machine-readable form in the [online article](#).)

**Table A7**  
Spectral Characteristic of ULGRBs Obtained from the Analysis of Fermi-LAT Observation

Fermi ID	Mission Elapsed Time (s)	Boresight (deg)	$\Gamma_{LAT}$	Energy Flux ( $\times 10^{-10}$ erg s $^{-1}$ cm $^{-2}$ )	Photon Flux ( $\times 10^{-6}$ Ph s $^{-1}$ cm $^{-2}$ )	TS
151027166	467,611,108.033	9	$-2.73 \pm 0.62$	$0.72 \pm 0.34$	$1.96 \pm 1.04$	17
170405777	513,110,367.886	52	$-2.61 \pm 0.36$	$0.46 \pm 0.15$	$1.16 \pm 0.36$	33
190114873	569,192,227.626	67	$-2.61 \pm 0.36$	$0.46 \pm 0.15$	$1.16 \pm 0.36$	16
210619999	645,839,970.604	109	$-1.42 \pm 0.27$	$0.45 \pm 0.22$	$0.24 \pm 0.15$	30
220101215	662,706,616.734	18	$-2.68 \pm 0.29$	$1.75 \pm 4.42$	$4.64 \pm 1.10$	61
220627890	678,057,665.086	27	$-2.19 \pm 0.16$	$5.35 \pm 1.12$	$9.14 \pm 1.70$	140
221009553	687,014,224.988	62	$-1.74 \pm 0.08$	$19.4 \pm 2.28$	$17.9 \pm 2.16$	494

(This table is available in machine-readable form in the [online article](#).)

sets were combined to obtain sky frames after preprocessing. After sky subtraction, we aligned the source images and conducted point-spread function photometry on the resulting stacked image. Early on, we observed the optical afterglow of

GRB 221009A on 2023 October 16, about 7 days after the burst, using the 1.3 m Devasthal Fast Optical Telescope at ARIES (Gupta et al. 2022d). We took multiple frames in the R band and used the Image Reduction and Analysis Facility

**Table A8**  
Summary of Initial and Final Parameters of Massive Star Models Simulated Using the MESA Code

$M_{\text{ZAMS}}$ ( $M_{\odot}$ )	$\Omega/\Omega_c$	$M_{\text{final}}$ ( $M_{\odot}$ )	$R_{\text{final}}$ ( $R_{\odot}$ )	$M_{\text{Fe-core}}$ ( $M_{\odot}$ )	$\log(T_{\text{eff}})$ (K)	$\text{Log}(L)$ ( $L_{\odot}$ )	$t_{\text{ff}}$ (s)	$t_b$ (s)
15	0.1	14.96	603.23	1.55	3.64	5.08	1,438,579.51	140.7
15	0.2	14.96	593.52	1.65	3.67	5.17	1,403,955.16	138.4
15	0.3	14.95	57.19	1.91	4.20	5.29	42,011.37	13.3
15	0.4	13.62	11.11	2.05	4.70	5.85	3768.59	2.6
15	0.5	13.42	10.51	1.90	4.71	5.83	3494.82	2.4
15	0.6	13.26	9.55	1.93	4.72	5.81	3043.96	2.2
20	0.1	19.97	549.77	1.59	3.70	5.25	1,083,359.66	128.2
20	0.2	19.92	488.37	1.96	3.76	5.39	908,098.89	113.9
20	0.3	18.22	12.93	2.05	4.70	5.98	4088.36	3.0
20	0.4	17.91	12.17	2.04	4.71	5.97	3769.02	2.8
20	0.5	17.60	12.43	1.94	4.70	5.96	3923.15	2.9
20	0.6	17.36	12.76	1.90	4.70	5.96	4110.22	3.0
25	0.1	24.91	489.57	1.98	3.79	5.50	815,131.60	114.2
25	0.2	24.83	662.72	1.98	3.77	5.70	1,285,760.38	154.6
25	0.3	22.42	12.98	1.93	4.72	6.07	3707.46	3.0
25	0.4	22.10	14.16	1.77	4.70	6.06	4256.61	3.3
25	0.5	21.50	13.01	1.91	4.72	6.05	3800.50	3.0
25	0.6	21.17	12.37	1.88	4.73	6.04	3552.95	2.9
30	0.1	29.89	77.90	1.91	4.23	5.65	47,233.24	18.2
30	0.2	29.76	72.49	1.82	4.29	5.82	42,492.10	16.9
30	0.3	26.62	14.31	1.86	4.72	6.15	3939.29	3.3
30	0.4	26.11	15.63	1.78	4.70	6.14	4540.96	3.6
30	0.5	25.44	14.31	1.79	4.72	6.13	4029.45	3.3
30	0.6	25.09	13.75	1.93	4.72	6.12	3820.44	3.2

**Notes.** Starting from the PMS, the models are evolved until they reach the stage of the onset of core collapse. Here,  $M_{\text{ZAMS}}$  is the mass of the model at ZAMS, and  $\Omega/\Omega_c$  is the ratio of initial angular rotational velocity and critical angular rotational velocity. Further, the  $M_{\text{final}}$  is the mass,  $R_{\text{final}}$  is the radius,  $M_{\text{Fe-core}}$  is the iron-core mass,  $T_{\text{eff}}$  is the effective temperature, and  $L$  is the corresponding luminosity of the model at the stage of the onset of core collapse. Additionally,  $t_{\text{ff}}$  and  $t_b$  are the freefall time of the star model and the bore-time of the weak jet, respectively.

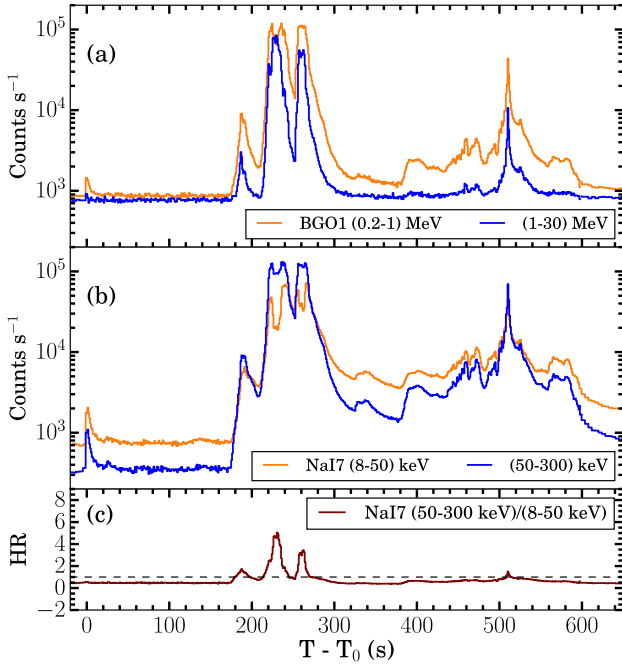


**Figure A1.** Fermi-GBM multichannel light curve of GRB 221009A. Panels (a) and (b) display the count-rate light curve in the two energy channels of the BGO and NaI scintillation detectors, respectively. (c) depicts the hardness ratio in the two energy channels of the NaI scintillation detector. The specific energy channels used are indicated in the legends.

(IRAF) to process the optical data (Gupta et al. 2022b). The magnitudes of the source obtained from our observations are listed in Table A5, and finding charts are shown in Figure A4.

In addition to our observations from the 3.6 m DOT of GRB 221009A, data points in various NIR-optical bands have been obtained from GCN,<sup>16</sup> as well as publications by Laskar et al. (2023), O’Connor et al. (2023), Shrestha et al. (2023), and R. Sánchez-Ramírez et al. (2024, in preparation) to get a well-sampled light curve. We obtained the Swift-XRT light curve at 10 keV from the official Swift webpage.<sup>17</sup> We employed the Markov Chain Monte Carlo fitting technique to model the afterglow light curves. We used a smoothly joined broken power law to fit the optical  $R$ -band light curve (good coverage) to determine the break time  $T_{\text{b,o}}$ . The smoothness parameter was fixed at 3. The fitting parameters obtained were  $\alpha_{\text{o},1} = 0.57^{+0.04}_{-0.04}$  and  $\alpha_{\text{o},2} = 1.43^{+0.02}_{-0.02}$ , with a break time  $T_{\text{b,o}} = 24700^{+2500}_{-2500}$ . The late-time light curves in other optical bands were fitted using a simple power-law function, and the resulting decay indices were consistent within the error bar of the postbreak decay index ( $\alpha_{\text{o},2}$ ) in the  $R$ -band light curve. We also observed an achromatic behavior in the optical and NIR light curves, with temporal decay indices of  $\alpha_J \sim 1.4$  and  $\alpha_K \sim 1.45$  in the  $J$  and  $K$  bands, respectively.

The light curve of GRB 221009A from Swift-XRT displays a smooth decay. We utilized a simple power-law function to fit

<sup>16</sup> <https://gcn.gsfc.nasa.gov/other/221009A.gcn3>

<sup>17</sup> [https://www.swift.ac.uk/burst\\_analyser/01126853/](https://www.swift.ac.uk/burst_analyser/01126853/)

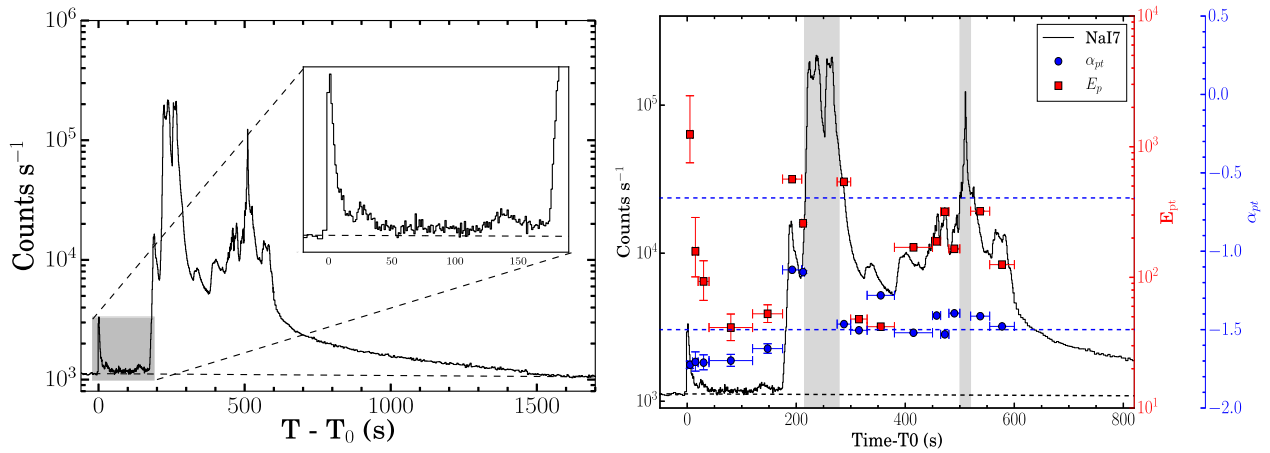


**Figure A2.** Left: Fermi-GBM light curve of GRB 221009A. The shaded area represents the quiescent phase, a zoomed version of which is shown in the inset. Right: the evolution of prompt emission spectral parameters  $E_{pt}$  (red squares) and  $\alpha_{pt}$  (blue circles) along the GBM light curve (black) is shown. The blue dashed lines at  $[-3/2, -2/3]$  represent the synchrotron line of death for low-energy spectral index  $\alpha_{pt}$ . Black dashed lines depict the background counts. Shaded areas represent the bad time intervals [217–280 s] and [508–514 s] Lesage et al. (2023) omitted in the spectral fitting.

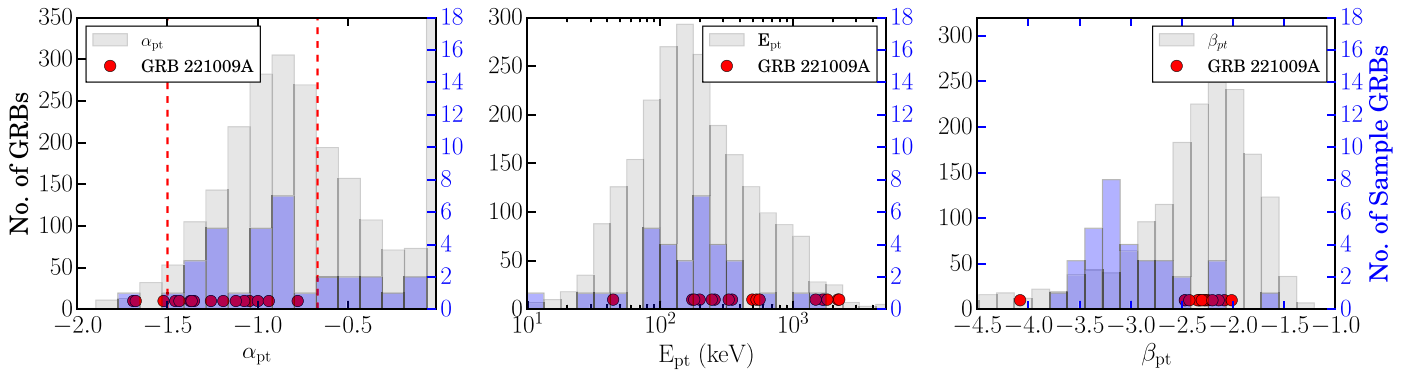


**Figure A3.** Left panel: distribution of  $\alpha_{pt}$  of the complete sample Fermi-detected GRBs (gray) along with those GRBs with Fermi-GBM detection (blue) in our selected sample. Similarly, the middle and right panels show the distribution of  $E_{pt}$  and  $\beta_{pt}$ , respectively. The red dots represent the distribution of parameters obtained from the time-resolved analysis of Fermi-GBM observation of GRB 221009A.

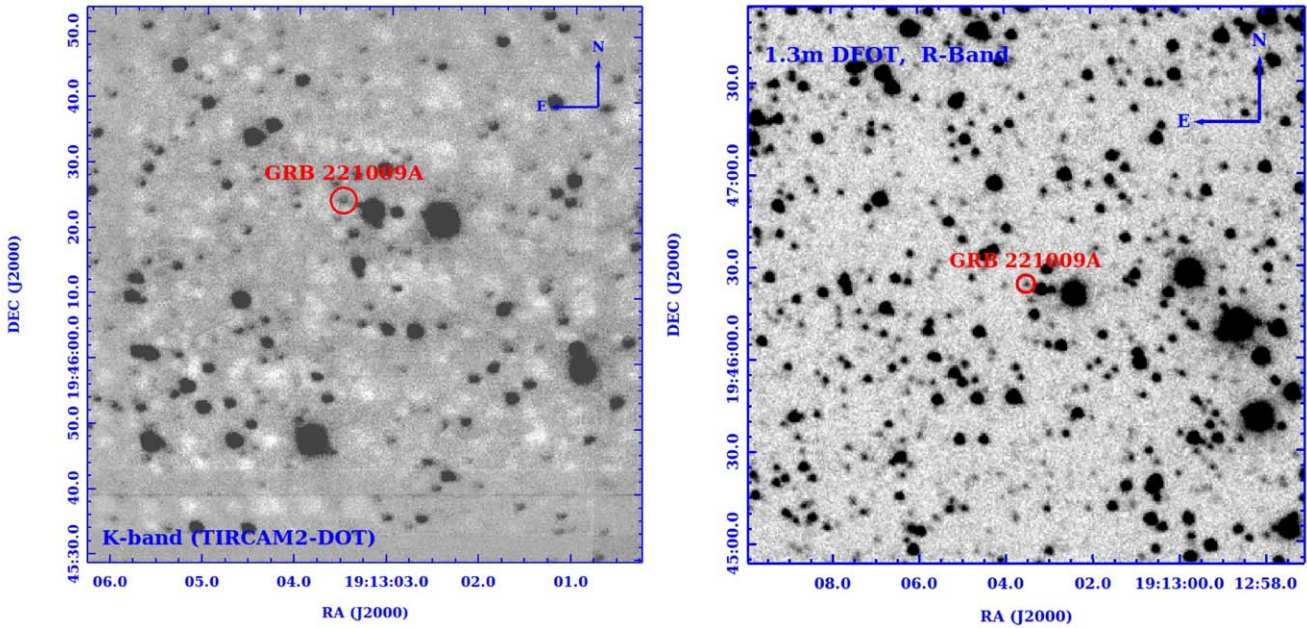


**Figure A4.** Left, the K-band finding chart for GRB 221009A from observations made with the TIRCAM2 instrument mounted on the side port of the 3.6 m DOT. Right, the R-band finding chart is generated from observations made with the 1.3 m DFOT.

it, yielding a decay index of  $\alpha_x = 1.66^{+0.01}_{-0.01}$  with BIC = 35120. Additionally, we attempted fitting the Swift-XRT light curve using the smoothly joined broken power law with the smoothness parameter fixed at 3 and constrain  $\alpha_{x,1} = 1.57^{+0.02}_{-0.02}$ ,  $\alpha_{x,2} = 1.86^{+0.02}_{-0.02}$ , and the break time  $T_{b,x} \sim 84,000^{+4500}_{-6500}$  s with BIC = 34,203. The smoothly joined broken power-law model provided a better fit with a lower BIC value ( $\Delta\text{BIC} < 900$ ) to the observed data.

### A.2.2. Spectral Energy Distribution Analysis and Closure Relations

To create the NIR-optical-X-ray spectral energy distribution (SED), we have used the methodology described in Gupta (2023) and Ror et al. (2023). We have retrieved the Swift-XRT spectra for GRB 221009A from the Swift webpage<sup>18</sup> at two epochs (corresponding to which we have enough NIR/optical observations). To model the XRT spectrum using XSPEC, we employed a power-law function combined with Galactic (phabs fixed at  $\text{NH}_{\text{Gal}} = 5.38 \times 10^{21} \text{ cm}^{-2}$ ) and intrinsic (zphabs) absorption components. To constrain the intrinsic hydrogen column density ( $\text{NH}_z$ ), we fitted the late-time spectra and found  $\text{NH}_z = 1.40 \times 10^{22} \text{ cm}^{-2}$ . We fixed  $\text{NH}_z$  for the spectral analysis and found X-ray spectral indices  $\beta_x = 0.80^{+0.04}_{-0.04}$ . The  $\beta_x$  obtained from our analysis is consistent with the results of Williams et al. (2023). We fit the NIR-optical observations with a simple power law to constrain the optical spectral indices ( $\beta_o$ ).

GRB afterglows are assumed to follow certain closure relations that help to constrain the spectral regime of the afterglow emission as well as the circumburst medium surrounding the burst (Sari et al. 1998; Gao et al. 2013). For GRB 221009A, we have studied several cases and found that the spectral and temporal indices obtained for different spectral regimes are not fully consistent with the existing closure relations. For  $p > 2$  case and in the spectral regime  $\nu_m < \nu_o < \nu_x < \nu_c$ , we have  $p = 2\beta + 1 \sim 2.6$ . The  $p$ -value obtained in this spectral regime for a Wind-like medium only explains the decay  $\alpha = (3p - 1)/4 = 1.7$  of the XRT light curve  $\alpha_x = 1.66 \pm 0.01$  but not the optical light curve  $\alpha_{o,2} = 1.43 \pm 0.02$  in  $5\sigma$  range. In an ISM-like medium, the  $\alpha = 3(p - 1)/4 = 1.2$  is again too shallow to explain the decay in optical and X-ray light curves. In the spectral regime  $\nu_m < \nu_c < \nu_o < \nu_x$ ,  $p = 2.6$  in both ISM and WIND-like media is able to explain the decay of optical light with decay index  $\alpha = (3p - 2)/4 = 1.45$  within  $1\sigma$ , but this is shallower than the decay of X-ray light curve. If we consider an early jet break, then, for  $p = 2.6$ , the decay indices obtained for the ISM and the WIND-like circumburst medium are much steeper than the observed values.

For  $p < 2$  cases,  $p = 2\beta \sim 1.6$ , without considering an early jet break. In the spectral regime  $\nu_m < \nu_o < \nu_x < \nu_c$ , the optical and XRT decay indices are not consistent with the closure relations  $\alpha = \frac{3(p+2)}{16} = 0.68$  and  $\alpha = \frac{(p+8)}{8} = 1.2$  for ISM and WIND-like circumburst medium, respectively. Similarly, for the spectral regime,  $\nu_m < \nu_c < \nu_o < \nu_x$ ,  $\alpha = \frac{(3p+10)}{16} = 0.92$  (ISM), and  $\alpha = \frac{(p+6)}{8} = 0.95$  (Wind) are again too shallow compared to optical and X-ray decay indices.

For  $p < 2$  with an early jet break, the optical decay indices are consistent with the relation  $\alpha = \frac{3(p+6)}{16} \sim 1.43$  in the ISM-like circumburst medium for the spectral regime

$\nu_m < \nu_o < \nu_c < \nu_x$ . The X-ray decay index within the same spectral regime is consistent with the relation  $\alpha = \frac{3p+22}{16} = 1.67$  within  $1\sigma$ .

Thus, if we consider a break in the Swift-XRT light curve, then these relations are feasible to explain the decay of the optical and XRT light curves; such a break and ISM-like medium are also consistent with the analysis of A. J. Levan et al. (2023) and O'Connor et al. (2023).

### A.3. Calculation of Bore-time ( $t_b$ ) for Three Different Scenarios

Utilizing Equation (1) with  $L_{\gamma,\text{iso}} = 9.91 \times 10^{53} \text{ erg s}^{-1}$  and  $\theta_j = 0.1 \text{ rad}$  ( $5.7^\circ$ ) (Kann et al. 2023; A. J. Levan et al. 2023; O'Connor et al. 2023), we have calculated the value of  $t_b$  for GRB 221009A for three different cases:

1. *R and M fixed.* For  $R = 10^{11} \text{ cm}$  and  $M = 15 M_\odot$ , we obtain  $T_{90}/t_b = 4270.76$ .
2. *R fixed M changed.* For  $R$  fixed at  $10^{11} \text{ cm}$  but  $M$  increased to  $30 M_\odot$ , we obtain  $T_{90}/t_b = 3390.494$ , i.e., there is 20% decrement in  $T_{90}/t_b$ .
3. *R and M, both changed.* Further, by varying the radius according to the relation,  $R = 1.33M^{0.55}$  corresponding to  $M = 30 M_\odot$ . We obtain the ratio  $T_{90}/t_b = 2635.142$ , i.e., 38% decrement to the initial value. These results are consistent with our analysis given in Section 4.2.

## ORCID iDs

Amit Kumar Ror  <https://orcid.org/0000-0003-3164-8056>  
 Rahul Gupta  <https://orcid.org/0000-0003-4905-7801>  
 Amar Aryan  <https://orcid.org/0000-0002-9928-0369>  
 S. R. Oates  <https://orcid.org/0000-0001-9309-7873>  
 A. J. Castro-Tirado  <https://orcid.org/0000-0003-2999-3563>  
 Sudhir Kumar  <https://orcid.org/0000-0003-1186-2119>

## References

- Abbott, B. P., Abbott, R., Abbott, T. D., et al. 2017, *ApJ*, 848, L13  
 Abdalla, H., Adam, R., Aharonian, F., et al. 2019, *Natur*, 575, 464  
 Aguilera-Dena, D. R., Langer, N., Moriya, T. J., & Schootemeijer, A. 2018, *ApJ*, 858, 115  
 Ahumada, T., Singer, L. P., Anand, S., et al. 2021, *NatAs*, 5, 917  
 Arimoto, M., Asano, K., Tachibana, Y., & Axelsson, M. 2020, *ApJ*, 891, 106  
 Arnaud, K. A. 1996, in ASP Conf. Ser. 101, *Astronomical Data Analysis Software and Systems V*, ed. G. H. Jacoby & J. Barnes (San Francisco, CA: ASP), 17  
 Aryan, A., Pandey, S. B., Gupta, R., & Ror, A. K. 2023, *MNRAS*, 521, L17  
 Aryan, A., Pandey, S. B., Zheng, W., et al. 2021, *MNRAS*, 505, 2530  
 Aryan, A., Pandey, S. B., Zheng, W., et al. 2022, *MNRAS*, 517, 1750  
 Barthelmy, S. D., Barbier, L. M., Cummings, J. R., et al. 2005, *SSRv*, 120, 143  
 Beniamini, P., Nava, L., Duran, R. B., & Piran, T. 2015, *MNRAS*, 454, 1073  
 Blanchard, P. K., Villar, V. A., Chornock, R., et al. 2024, *NatAs*, 8, 774  
 Blandford, R. D., & McKee, C. F. 1976, *PhFl*, 19, 1130  
 Blandford, R. D., & Znajek, R. L. 1977, *MNRAS*, 179, 433  
 Bloom, J. S., van Dokkum, P. G., Bailyn, C. D., et al. 2004, *AJ*, 127, 252  
 Boër, M., Gendre, B., & Stratta, G. 2015, *ApJ*, 800, 16  
 Bromberg, O., Nakar, E., & Piran, T. 2011, *ApJL*, 739, L55  
 Bromberg, O., Nakar, E., Piran, T., & Sari, R. 2013, *ApJ*, 764, 179  
 Bucciantini, N., Quataert, E., Arons, J., Metzger, B. D., & Thompson, T. A. 2007, *MNRAS*, 380, 1541  
 Bucciantini, N., Quataert, E., Metzger, B. D., et al. 2009, *MNRAS*, 396, 2038  
 Burns, E., Svinkin, D., Fenimore, E., et al. 2023, *ApJL*, 946, L31  
 Caballero-García, M. D., Gupta, R., Pandey, S. B., et al. 2023, *MNRAS*, 519, 3201  
 Campana, S., Lodato, G., D'Avanzo, P., et al. 2011, *Natur*, 480, 69  
 Campana, S., Mangano, V., Blustin, A. J., et al. 2006, *Natur*, 442, 1008

<sup>18</sup> [https://www.swift.ac.uk/xrt\\_spectra/01126853/](https://www.swift.ac.uk/xrt_spectra/01126853/)

- Campana, S., Thöne, C. C., de Ugarte Postigo, A., et al. 2010, *MNRAS*, **402**, 2429
- Cano, Z., de Ugarte Postigo, A., Pozanenko, A., et al. 2014, *A&A*, **568**, A19
- Cano, Z., Izzo, L., de Ugarte Postigo, A., et al. 2017, *A&A*, **605**, A107
- Chen, J.-M., Peng, Z.-Y., Du, T.-T., Yin, Y., & Wu, H. 2021, *ApJ*, **920**, 53
- Cucchiara, A., Veres, P., Corsi, A., et al. 2015, *ApJ*, **812**, 122
- Dagoneau, N., Schanne, S., Atteia, J.-L., Götz, D., & Cordier, B. 2020, *ExA*, **50**, 91
- Dalton, T., & Morris, S. L. 2020, *MNRAS*, **495**, 2342
- de Ugarte Postigo, A., Horváth, I., Veres, P., et al. 2011, *A&A*, **525**, A109
- de Ugarte Postigo, A., Izzo, L., Thoené, C. C., et al. 2022, GCN, 32800
- de Wet, S., Izzo, L., Groot, P. J., et al. 2023, *A&A*, **677**, A32
- Demircan, O., & Kahraman, G. 1991, *Ap&SS*, **181**, 313
- Dessart, L., & Hillier, D. J. 2018, arXiv:1812.07620
- Dichiara, S., Gropp, J. D., Kennea, J. A., et al. 2022, GCN, 32632
- Evans, P. A., Beardmore, A. P., Page, K. L., et al. 2007, *A&A*, **469**, 379
- Evans, P. A., Beardmore, A. P., Page, K. L., et al. 2009, *MNRAS*, **397**, 1177
- Evans, P. A., Willingale, R., Osborne, J. P., et al. 2014, *MNRAS*, **444**, 250
- Farmer, R., Fields, C. E., Petermann, I., et al. 2016, *ApJS*, **227**, 22
- Frajna, N., Dichiara, S., & Pedreira, A. C. C. d. E. S. 2019, *ApJL*, **879**, L26
- Frajna, N., Gonzalez, M., & HAWC Collaboration 2022, ATel, 15675
- Frederiks, D., Svinkin, D., Lysenko, A. L., et al. 2023, *ApJL*, **949**, L7
- Fulton, M. D., Smartt, S. J., Rhodes, L., et al. 2023, *ApJL*, **946**, L22
- Galama, T. J., Vreeswijk, P. M., van Paradijs, J., et al. 1998, *Natur*, **395**, 670
- Gao, H., Lei, W.-H., Zou, Y.-C., Wu, X.-F., & Zhang, B. 2013, *NewAR*, **57**, 141
- García-Cifuentes, K., Becerra, R. L., De Colle, F., Cabrera, J. I., & Del Burgo, C. 2023, *ApJ*, **951**, 4
- Garnavich, P. M., Stanek, K. Z., Wyrzykowski, L., et al. 2003, *ApJ*, **582**, 924
- Gehrels, N., Chincarini, G., Giommi, P., et al. 2004, *ApJ*, **611**, 1005
- Gendre, B., Joyce, Q. T., Orange, N. B., et al. 2019, *MNRAS*, **486**, 2471
- Goldstein, A., Cleveland, W. H., & Kocevski, D., 2022 Fermi GBM Data Tools: v1.1.1., <https://fermi.gsfc.nasa.gov/ssc/data/analysis/gbm>
- Golenetskii, S. V., Mazets, E. P., Aptekar, R. L., & Ilinskii, V. N. 1983, *Natur*, **306**, 451
- Gottlieb, O., Lalakos, A., Bromberg, O., Liska, M., & Tchekhovskoy, A. 2022, *MNRAS*, **510**, 4962
- Greiner, J., Mazzali, P. A., Kann, D. A., et al. 2015, *Natur*, **523**, 189
- Gupta, R. 2023, arXiv:2312.16265
- Gupta, R., Gupta, S., Chattopadhyay, T., et al. 2022a, *MNRAS*, **511**, 1694
- Gupta, R., Kumar, A., Pandey, S. B., et al. 2022b, *JApA*, **43**, 11
- Gupta, R., Oates, S. R., Pandey, S. B., et al. 2021a, *MNRAS*, **505**, 4086
- Gupta, R., Pandey, S. B., Castro-Tirado, A. J., et al. 2021b, *RMxAC*, **53**, 113
- Gupta, R., Pandey, S. B., Kumar, A., et al. 2022c, *JApA*, **43**, 82
- Gupta, R., Pandey, S. B., Ror, A. K., Aryan, A., & Tiwari, S. N. 2024, *BSRSL*, **93**, 683
- Gupta, R., Ror, A. K., Pandey, S. B., et al. 2022d, GCN, 32811
- Henyey, L., Vardya, M. S., & Bodenheimer, P. 1965, *ApJ*, **142**, 841
- Hewig, F. 2000, *A&A*, **360**, 952
- Hjorth, J., Sollerman, J., Møller, P., et al. 2003, *Natur*, **423**, 847
- Holland, S. T., Sbarufatti, B., Shen, R., et al. 2010, *ApJ*, **717**, 223
- Hou, S.-J., Liu, T., Xu, R.-X., et al. 2018, *ApJ*, **854**, 104
- Hu, Y. D., Castro-Tirado, A. J., Kumar, A., et al. 2021, *A&A*, **646**, A50
- Huang, Y., Hu, S., Chen, S., et al. 2022, GCN, 32677
- Huang, Y.-Y., Zhang, H.-M., Yan, K., Liu, R.-Y., & Wang, X.-Y. 2022, *ApJL*, **940**, L36
- Hunter, J. D. 2007, *CSE*, **9**, 90
- Ioka, K., Hotokezaka, K., & Piran, T. 2016, *ApJ*, **833**, 110
- Jermyn, A. S., Bauer, E. B., Schwab, J., et al. 2023, *ApJS*, **265**, 15
- Jespersen, C. K., Severin, J. B., Steinhart, C. L., et al. 2020, *ApJL*, **896**, L20
- Jin, Z.-P., Covino, S., Della Valle, M., et al. 2013, *ApJ*, **774**, 114
- Kann, D. A., Agayeva, S., Aivazyan, V., et al. 2023, *ApJL*, **948**, L12
- Kann, D. A., Klose, S., Zhang, B., et al. 2010, *ApJ*, **720**, 1513
- Kann, D. A., Schady, P., Olivares, E. F., et al. 2018, *A&A*, **617**, A122
- Kennea, J. A., & Williams, M. 2022, GCN, 32635
- Kippenhahn, R., Ruschenplatt, G., & Thomas, H. C. 1980, *A&A*, **91**, 175
- Klose, S., Schmidl, S., Kann, D. A., et al. 2019, *A&A*, **622**, A138
- Kocevski, D., Modjaz, M., Bloom, J. S., et al. 2007, *ApJ*, **663**, 1180
- Kouveliotou, C., Meegan, C. A., Fishman, G. J., et al. 1993, *ApJL*, **413**, L101
- Kumar, A., Pandey, S. B., Gupta, R., et al. 2022, *NewA*, **97**, 101889
- Kumar, P., & Barniol Duran, R. 2009, *MNRAS*, **400**, L75
- Kumar, P., & Barniol Duran, R. 2010, *MNRAS*, **409**, 226
- Kumar, P., & Zhang, B. 2015, *PhR*, **561**, 1
- Lan, L., Gao, H., Li, A., et al. 2023, *ApJL*, **949**, L4
- Langer, N., El Eid, M. F., & Fricke, K. J. 1985, *A&A*, **145**, 179
- Laros, J. G., Evans, W. D., Fenimore, E. E., et al. 1985, *ApJ*, **290**, 728
- Larsson, J., Levan, A. J., Davies, M. B., & Fruchter, A. S. 2007, *MNRAS*, **376**, 1285
- Laskar, T., Alexander, K. D., Margutti, R., et al. 2023, *ApJL*, **946**, L23
- Le Floch, E., Duc, P. A., Mirabel, I. F., et al. 2003, *A&A*, **400**, 499
- Lesage, S., Veres, P., Briggs, M. S., et al. 2023, *ApJL*, **952**, L42
- Levan, A., Gompertz, B. P., Salafia, O. S., et al. 2024, *Natur*, **626**, 737
- Levan, A. J. 2015, *JHEAp*, **7**, 44
- Levan, A. J., Lamb, G. P., Schneider, B., et al. 2023, *ApJL*, **946**, L28
- Levan, A. J., Tanvir, N. R., Starling, R. L. C., et al. 2014, *ApJ*, **781**, 13
- Li, L., Wu, X.-F., Lei, W.-H., et al. 2018, *ApJS*, **236**, 26
- Li, L.-X. 2007, *MNRAS*, **380**, 621
- Lien, A., Sakamoto, T., Barthelmy, S. D., et al. 2016, *ApJ*, **829**, 7
- Lin, D.-B., Lu, R.-J., Du, S.-S., et al. 2019, *ApJ*, **883**, 187
- Liu, R.-Y., Zhang, H.-M., & Wang, X.-Y. 2023, *ApJL*, **943**, L2
- Lü, H.-J., & Zhang, B. 2014, *ApJ*, **785**, 74
- Lyman, J. D., Levan, A. J., Tanvir, N. R., et al. 2017, *MNRAS*, **467**, 1795
- MAGIC Collaboration, Acciari, V. A., Ansoldi, S., et al. 2019, *Natur*, **575**, 459
- Mannucci, F., Salvaterra, R., & Campisi, M. A. 2011, *MNRAS*, **414**, 1263
- Meegan, C., Lichti, G., Bhat, P., et al. 2009, *ApJ*, **702**, 791
- Mei, A., Oganessian, G., Tsvetkova, A., et al. 2022, *ApJ*, **941**, 82
- Mészáros, P. 2006, *RPPh*, **69**, 2259
- Moss, M., Lien, A., Guiriec, S., Cenko, S. B., & Sakamoto, T. 2022, *ApJ*, **927**, 157
- Nakauchi, D., Kashiyama, K., Suwa, Y., & Nakamura, T. 2013, *ApJ*, **778**, 67
- Norris, J. P., Share, G. H., Messina, D. C., et al. 1986, *ApJ*, **301**, 213
- Nugent, A. E., Fong, W.-F., Dong, Y., et al. 2022, *ApJ*, **940**, 57
- O'Connor, B., Troja, E., Ryan, G., et al. 2023, *SciA*, **9**, eadi1405
- Olivares, E. F., Greiner, F., & Schady, J. 2015, *A&A*, **577**, A44
- Pandey, S. B. 2016, *RMxAC*, **48**, 83
- Pandey, S. B. 2018, in Proc. of the Int. Conf., SN 1987A, Quark Phase Transition in Compact Objects and Multimessenger Astronomy, **149**
- Paxton, B., Bildsten, L., Dotter, A., et al. 2011, *ApJS*, **192**, 3
- Paxton, B., Cantiello, M., Arras, P., et al. 2013, *ApJS*, **208**, 4
- Paxton, B., Marchant, P., Schwab, J., et al. 2015, *ApJS*, **220**, 15
- Paxton, B., Schwab, J., Bauer, E. B., et al. 2018, *ApJS*, **234**, 34
- Paxton, B., Smolec, R., Schwab, J., et al. 2019, *ApJS*, **243**, 10
- Pe'er, A. 2015, *AdAst*, **2015**, 907321
- Peng, F.-k., Hu, Y.-D., Xi, S.-Q., et al. 2013, arXiv:1302.4876
- Perley, D. A., Cenko, S. B., Corsi, A., et al. 2014, *ApJ*, **781**, 37
- Perley, D. A., Levan, A. J., Tanvir, N. R., et al. 2013, *ApJ*, **778**, 128
- Perna, R., & Belczynski, K. 2002, *ApJ*, **570**, 252
- Perna, R., Lazzati, D., & Cantiello, M. 2018, *ApJ*, **859**, 48
- Piran, T., & Nakar, E. 2010, *ApJL*, **718**, L63
- Preece, R. D., Briggs, M. S., Giblin, T. W., et al. 2002, *ApJ*, **581**, 1248
- Price, P. A., Berger, E., Reichart, D. E., et al. 2002, *ApJL*, **572**, L51
- Qian, Y. Z., & Woosley, S. E. 1996, *ApJ*, **471**, 331
- Ror, A. K., Gupta, R., Jelinek, M., et al. 2023, *ApJ*, **942**, 34
- Ruffini, R., Becerra, L., Bianco, C. L., et al. 2018, *ApJ*, **869**, 151
- Sari, R., Piran, T., & Narayan, R. 1998, *ApJ*, **497**, L17
- Schady, P., Page, M. J., Oates, S. R., et al. 2010, *MNRAS*, **401**, 2773
- Schroeder, G., Laskar, T., Fong, W.-F., et al. 2022, *ApJ*, **940**, 53
- Schulze, S., Malesani, D., Cucchiara, A., et al. 2014, *A&A*, **566**, A102
- Sharma, V., Iyyani, S., & Bhattacharya, D. 2021, *ApJL*, **908**, L2
- Shrestha, M., Sand, D. J., Alexander, K. D., et al. 2023, *ApJL*, **946**, L25
- Song, C.-Y., & Liu, T. 2023, *ApJ*, **952**, 156
- Song, X.-Y., & Zhang, S.-N. 2023, *ApJ*, **957**, 31
- Starling, R. L. C., Wiersema, K., Levan, A. J., et al. 2011, *MNRAS*, **411**, 2792
- Stetson, P. B. 1987, *PASP*, **99**, 191
- Tanvir, N. R., Fynbo, J. P. U., de Ugarte Postigo, A., et al. 2019, *MNRAS*, **483**, 5380
- Thöne, C. C., de Ugarte Postigo, A., Fryer, C. L., et al. 2011, *Natur*, **480**, 72
- Tody, D. 1986, *Proc. SPIE*, **627**, 733
- Tody, D. 1993, in ASP Conf. Ser. 52, Astronomical Data Analysis Software and Systems II, ed. R. J. Hanisch, R. J. V. Brissenden, & J. Barnes (San Francisco, CA: ASP), **173**
- Toy, V. L., Cenko, S. B., Silverman, J. M., et al. 2016, *ApJ*, **818**, 79
- Troja, E., Fryer, C. L., O'Connor, B., et al. 2022, *Natur*, **612**, 228
- Usov, V. V. 1992, *Natur*, **357**, 472
- van der Horst, A. J., Levan, A. J., Pooley, G. G., et al. 2015, *MNRAS*, **446**, 4116
- Vianello, G., Lauer, R. J., Younk, P., et al. 2015, arXiv:1507.08343
- Virgili, F. J., Mundell, C. G., Pal'shin, V., et al. 2013, *ApJ*, **778**, 54
- Wang, F. Y., & Dai, Z. G. 2014, *ApJS*, **213**, 15
- Williams, M. A., Kennea, J. A., Dichiara, S., et al. 2023, *ApJL*, **946**, L24
- Woosley, S. E. 1993, *ApJ*, **405**, 273

Xin, L. P., Zheng, W. K., Wang, J., et al. 2010, [MNRAS](#), 401, 2005  
Yoon, S. C., & Langer, N. 2005, [A&A](#), 443, 643  
Yoon, S. C., Langer, N., & Norman, C. 2006, [A&A](#), 460, 199  
Zafar, T., Watson, D., Møller, P., et al. 2018, [MNRAS](#), 479, 1542

Zhang, B., Liang, E., Page, K. L., et al. 2007, [ApJ](#), 655, 989  
Zhang, B.-B., Zhang, B., Murase, K., Connaughton, V., & Briggs, M. S. 2014, [ApJ](#), 787, 66  
Zhang, H.-M., Huang, Y.-Y., Liu, R.-Y., & Wang, X.-Y. 2023, [ApJL](#), 956, L21